

THE ULTRA-LUMINOUS X-RAY SOURCE POPULATION FROM THE CHANDRA ARCHIVE OF GALAXIES

DOUGLAS A. SWARTZ¹, KAJAL K. GHOSH¹, ALLYN F. TENNANT², KINWAH WU³

Draft version August 23, 2018

ABSTRACT

One hundred fifty-four discrete non-nuclear Ultra-Luminous X-ray (ULX) sources, with spectroscopically-determined intrinsic X-ray luminosities $> 10^{39}$ ergs s⁻¹, are identified in 82 galaxies observed with *Chandra*'s Advanced CCD Imaging Spectrometer. Source positions, X-ray luminosities, and spectral and timing characteristics are tabulated. Statistical comparisons between these X-ray properties and those of the weaker discrete sources in the same fields (mainly neutron star and stellar-mass black hole binaries) are made. Sources above $\sim 10^{38}$ ergs s⁻¹ display similar spatial, spectral, color, and variability distributions. In particular, there is no compelling evidence in the sample for a new and distinct class of X-ray object such as the intermediate-mass black holes. 83% of ULX candidates have spectra that can be described as absorbed power laws with index $\langle \Gamma \rangle = 1.74$ and column density $\langle N_H \rangle = 2.24 \times 10^{21}$ cm⁻², or ~ 5 times the average Galactic column. About 20% of the ULXs have much steeper indices indicative of a soft, and likely thermal, spectrum. The locations of ULXs in their host galaxies are strongly peaked towards their galaxy centers. The deprojected radial distribution of the ULX candidates is somewhat steeper than an exponential disk, indistinguishable from that of the weaker sources. About 5–15% of ULX candidates are variable during the *Chandra* observations (which average 39.5 ks). Comparison of the cumulative X-ray luminosity functions of the ULXs to *Chandra* Deep Field results suggests $\sim 25\%$ of the sources may be background objects including 14% of the ULX candidates in the sample of spiral galaxies and 44% of those in elliptical galaxies implying the elliptical galaxy ULX population is severely compromised by background active galactic nuclei. Correlations with host galaxy properties confirm the number and total X-ray luminosity of the ULXs are associated with recent star formation and with galaxy merging and interactions. The preponderance of ULXs in star-forming galaxies as well as their similarities to less-luminous sources suggest they originate in a young but short-lived population such as the high-mass X-ray binaries with a smaller contribution (based on spectral slope) from recent supernovae. The number of ULXs in elliptical galaxies scales with host galaxy mass and can be explained most simply as the high-luminosity end of the low-mass X-ray binary population.

Subject headings: galaxies: general — surveys — X-rays: binaries — X-rays: galaxies — X-rays: general

1. INTRODUCTION

Among the most intriguing objects in the X-ray sky are the discrete non-nuclear Ultra-Luminous X-ray sources (ULXs) in nearby galaxies. This name describes sources considerably more luminous than expected for a spherically-accreting object of typical neutron star mass. Here, ULXs are defined to be those with apparent (i.e., assumed isotropically emitting) intrinsic luminosities in excess of 10^{39} ergs s⁻¹ in the 0.5–8.0 keV bandpass.

Einstein X-ray images of galaxies revealed 16 ULX candidates (Long & Van Speybroeck 1983; Helfand 1984; Fabbiano 1989). *ROSAT* has extended this list to nearly 100 (Roberts & Warwick 2000; Colbert & Ptak 2002). Yet these objects are rare, reported at a rate of only 1–2 per galaxy from pointed X-ray observations (Colbert et al. 2004; Kilgard et al. 2002; Colbert & Ptak 2002; Foschini et al. 2002; Humphrey et al. 2003; Irwin, Athey, & Bregman 2003) and perhaps occurring much less frequently in the nearby Universe as a whole (Ptak & Colbert 2004). ULXs may represent the high-luminosity end

of a continuous distribution of typical X-ray sources such as supernovae and X-ray binaries (e.g., Grimm, Glifanov, & Sunyaev 2003) or they may include new classes of objects including intermediate mass black holes (Colbert & Mushotzky 1999; Makishima et al. 2000; Colbert & Ptak 2002; van der Marel 2004), beamed sources (King et al. 2001; Georganopoulos et al. 2002; Körding, Falcke, & Markoff 2002), and hypernovae (Wang 1999).

Part of the reason ULXs are, as a class, poorly understood is that past X-ray observatories lack the combination of high angular resolution and moderate spectral resolution needed to adequately characterize discrete X-ray sources in nearby galaxies. The highest spatial resolution instruments aboard both *Einstein* and *ROSAT* provide little or no spectral information and their spectroscopic instruments have poor angular resolution. The *ASCA* satellite provides moderate spectral resolution but very poor angular resolution. As a result, ULXs are difficult to resolve from other nearby X-ray sources and from diffuse emission in the field; their positions and morphologies are poorly known thus impeding follow-up investigations in other wavebands; and ULX X-ray spectra and timing properties are often sparsely sampled.

We have undertaken an extensive X-ray spectrophotometric survey of the discrete source populations in nearby galaxy fields anchored upon archival data obtained with

¹ Universities Space Research Association, NASA Marshall Space Flight Center, SD50, Huntsville, AL, USA

² Space Science Department, NASA Marshall Space Flight Center, SD50, Huntsville, AL, USA

³ MSSL, University College London, Holmbury St. Mary, Surrey, RH5 6NT, UK

the *Chandra* X-ray Observatory Advanced CCD Imaging Spectrometer (ACIS). The main goal of the survey is to systematically search for and evaluate the physical properties of ULXs. The survey encompasses a sample of ULXs large enough for meaningful statistical analyses; the survey is based upon high spatial resolution images that provide accurate celestial positions as well as medium-resolution broad-band spectral signatures and time sampling. The galaxies included in the survey span the range of Hubble morphological types and include galaxies of various mass, gas content, dynamical state, and evolutionary history; thus allowing correlations between ULXs and their local environments to be studied.

The galaxy selection process and the methods of X-ray data reduction and analysis are described in §2. The resulting sample of galaxies, their properties, and the properties of the ULX candidates are given in §3. The implications of the current survey for contemporary physical models for the ULX phenomena is discussed in §4.

2. METHODS

2.1. Galaxy Selection

Chandra/ACIS, operating in imaging mode, provides moderate spectral resolution and throughput at the highest spatial resolution available in an X-ray telescope facility. As our primary goals are to obtain accurate celestial positions and to perform spectroscopic analysis of ULX candidates, ACIS is the ideal instrument for the present study. To achieve these goals requires a minimum of ~ 50 X-ray counts per source distributed over several spectral energy bins. Thus, our sample includes nearly all available non-grating, timed exposure mode, ACIS galaxy observations (those listing a galaxy or a supernova as a target in the *Chandra* approved target lists⁴) publicly-available c. May 2003 with $\gtrsim 50$ counts expected from sources with intrinsic 0.5–8.0 keV luminosities of $L_X = 10^{39}$ ergs s⁻¹. NGC 221, NGC 224, and the Magellanic Clouds are the only galaxies purposely excluded from the sample. These galaxies are known to contain no ULXs and require multiple pointings for full coverage (except for the dwarf elliptical NGC 221). There were no non-targeted galaxies in the *Chandra* fields that met the selection criterion.

For each candidate galaxy in the archive, the number of counts expected from a ULX was estimated using the Portable Interactive Multi-Mission Simulator (PIMMS, Mukai 1993); the distance, D , to the galaxy; the duration, t , of the observation; and assuming an absorbed power law spectral shape with spectral index $\Gamma = 1.6$ and with a hydrogen column density, N_H , equal to the Galactic column density along the line of sight. The ACIS count rate for this spectral shape is $\sim 10^{-4}$ c s⁻¹ for a source flux of 10^{-15} ergs cm⁻² s⁻¹ (for a source imaged on the back-side illuminated CCDs in the 0.5–8.0 keV band and for a typical $N_H/10^{20} \sim 1$ –10 cm⁻². The count rate is about 30% lower if the source is imaged on the front-illuminated CCDs.) Thus, the requirement of 50 c from a source with luminosity $L_X = 10^{39}$ ergs s⁻¹ can be expressed as $t/D^2 \gtrsim 60$ where D is measured in Mpc. Typical ACIS observations are ~ 50 ks duration; limiting the distances to host galaxies to $\lesssim 30$ Mpc ($\lesssim 13$ Mpc for

a 10 ks observation).

Distances to the host galaxies were obtained from the literature. In order of preference, distances are based on the Cepheid period-luminosity relation ($\sim 5\%$ distance uncertainty; see Ferrarese et al. 2000), I -band surface brightness fluctuations (SBF, 10% uncertainty), on the tip of the red giant branch (10%), or on planetary nebula luminosity functions (10%). Distances based on globular cluster luminosity functions and K' and K_s -band SBF methods are somewhat more uncertain (Ferrarese et al. 2000). In a few cases, distances were based on tertiary distance indicators such as the brightest blue stars (see de Vaucouleurs 1978; Karachentsev & Tikhonov 1994 for definitions) and only recent, well-calibrated, distances were deemed reliable. Finally, distances tabulated in the catalogue of Tully (1988) were used when no other estimate was available. This catalogue uses the Virgo infall model of Tully & Shaya (1984), a variant of the Tully-Fisher relation, that assumes an infall velocity of 300 km s⁻¹ for the Local Group, $H_0 = 75$ km s⁻¹ Mpc⁻¹, and a Virgo distance of 16.8 Mpc. Distances in the Tully catalogue are most reliable for galaxies beyond Virgo.

The duration of the observations, t , were taken from the good-time intervals provided as part of the X-ray event lists. Galactic hydrogen column densities along the line-of-sight to the host galaxies were taken from the HI map of Dickey & Lockman (1990) using the FTOOL utility `nh` available from HEASARC.

2.2. Basic Galaxy Properties

Several global properties of the host galaxies were obtained to aid in data reduction and for subsequent analysis. Galaxy morphological type, major isophotal angular diameter ($\equiv D_{25}$, measured at surface brightness level 25.0 mag sec⁻² in blue light), major-to-minor isophotal diameter ratio, position angle of the major axis, galactic latitude, total (asymptotic) B -band magnitudes corrected for extinction and redshift, and $(B - V)$ colors are all taken from the Third Reference Catalogue of Bright Galaxies (de Vaucouleurs et al. 1991, hereafter RC3). The absolute B magnitudes, M_B , were derived from the apparent magnitudes and the adopted distances and converted to luminosities, L_B , using the standard photometric quantities cited in Zombeck (1990). Galaxy center coordinates were taken from the NASA/IPAC Extragalactic Database (NED) and are often based on accurate radio measurements. Typically, these values differ by no more than a few seconds of arc from those reported in RC3.

2.2.1. Far-Infrared Luminosities

Far-infrared measurements of the host galaxies made by the *Infrared Astronomical Satellite* (IRAS) were used to derive the far-infrared luminosities of galaxies in the sample. The total flux between 42.4 and 122.5 μ m is approximated by $1.26 \times 10^{-11} (2.58 S_{60} + S_{100})$ ergs cm⁻² s⁻¹ where S_{60} and S_{100} are the total flux densities at the 60 and 100 μ m bands, respectively (Rice et al. 1988). Flux densities were taken, in order of preference, from the tabulations in Ho, Filippenko, & Sargent (1997), Rice et al. (1988), Knapp et al. (1989), or from NED.

2.2.2. Nearest Neighbor Distances

⁴ http://asc.harvard.edu/target_lists

The separation between each host galaxy and its nearest neighbor was taken from the work of Ho, Filippenko, & Sargent (1997) or directly from NED. We define nearest neighbor to be the closest galaxy on the sky with a small relative velocity between the pair ($\Delta v \lesssim 500 \text{ km s}^{-1}$). The projected angular nearest-neighbor separation, θ_P , quoted in this work is given in units of the D_{25} isophotal angular diameter.

2.3. X-ray Data Reduction

For each X-ray observation, events within the D_{25} isophote were extracted from Level 2 event lists for analysis. For events on CCD S4, the `destreak` algorithm⁵ was applied to remove charge randomly deposited along pixel rows during readout and data from all CCDs were cleaned of bad pixels and columns. X-ray sources were then located and source spectra and time series for events within an $\sim 90\%$ encircled energy radius were extracted along with a background spectrum in a surrounding annulus for all sources with estimated luminosities exceeding $\sim 10^{38} \text{ ergs s}^{-1}$. (These estimates were based on the number of detected counts and assume the same spectral shapes as was used for galaxy selection, §2.1). Some details of the source finding algorithm are given in Swartz et al. (2003). The source and background region image, spectrum, and light curve were then visually inspected for anomalies such as background flares or other sources overlapping the extraction regions and appropriate adjustments made. Sources located within $5''$ of the host galaxy nucleus are not further considered in this work. X-ray source positions were mapped to second-generation Digitized Sky Survey blue (roughly 400–550 nm) images of the galaxies in order to identify and reject bright (above $\sim 20 \text{ mag}$) foreground stars based on spatial coincidence. Further analysis of non-X-ray data is in progress and will be reported elsewhere. In the few cases where more than one compatible observation of a galaxy was available, datasets were merged using FTOOL utilities to increase signal-to-noise.

2.3.1. Spectral Analysis

The XSPEC (v.11.2) spectral-fitting package was used for analysis of events in PI channels corresponding to 0.5 to 8.0 keV. Spectra were binned as needed to obtain at least 20 counts per fitting bin (before background subtraction) to ensure applicability of the χ^2 statistic. For sources resulting in fewer than 5 degrees of freedom, the unbinned spectra (without background subtracted) were also fit using the C-statistic to check for fit parameter consistency. Redistribution matrices and ancillary response files were generated using *Chandra* X-ray Center tools and calibration data (CIAO version 2.3) using the most recent gain maps and observation-specific bad pixel lists and aspect histories.

For sources imaged on front-side illuminated ACIS CCDs, the algorithm developed by Townsley et al. (2000) was applied to partially correct for the effects of charge loss and smearing caused by charge-transfer inefficiency. The algorithm was applied to the Level 1 event list, a new Level 2 file generated (following the CIAO threads), and the spectra re-extracted.

The `acisabs`⁶ correction was applied (as a multiplicative model in XSPEC) in all spectral fits to account for the temporal decrease in the low-energy sensitivity of the ACIS detectors. Sources with detected count rates in excess of 0.1 c frame^{-1} were treated for effects of pileup following the procedures described in Davis (2002) and using the event pileup model of Davis (2001). No CTI-correction was applied to piled-up spectra.

For each model, the fit parameters, 0.5–8.0 keV model flux, χ^2 statistic and number of degrees of freedom, and corresponding errors were recorded. All errors are extremes on the single interesting parameter 90% confidence intervals except for derived fluxes (and corresponding luminosities) where the 1σ errors are quoted. XSPEC-determined fluxes (see § 2.3.2), averaged over the duration of the observation, were then scaled by the inverse of the fraction of the telescope point spread function (PSF) within the source extraction region and luminosities computed using the adopted distances to the host galaxies.

X-ray sources in each galaxy field were sorted by number of detected counts. Spectral fits were then made beginning with the highest-count sources and continuing with lower-count sources until all potential ULX candidates were examined. This resulted in spectral fits for many sources with luminosities $< 10^{39} \text{ ergs s}^{-1}$.

In addition to fitting models to the 0.5–8.0 keV spectrum of the highest-count sources, the background-subtracted X-ray counts for all extracted sources were binned into three broad bands; defined as *S* (0.5–1.0 keV), *M* (1.0–2.0 keV), and *H* (2.0–8.0 keV); and the X-ray colors $(M - S)/T$ and $(H - M)/T$, where $T = S + M + H$, were constructed following Prestwich et al. (2003).

2.3.2. Determining ULX Status Spectroscopically

By our definition, a ULX is a discrete source whose *intrinsic* luminosity exceeds $10^{39} \text{ ergs s}^{-1}$ in the 0.5–8.0 keV energy band. An absorbed (multiplicative `acisabs` and `phabs` components) XSPEC-specific power law model called `pegpwrlw` was applied to the X-ray spectra to obtain the intrinsic luminosity. The normalization parameter for this model is the intrinsic flux in a prescribed bandpass. The uncertainty estimate for this parameter then provides the uncertainty in the intrinsic flux. The *observed* flux and corresponding uncertainty were obtained using XSPEC's `flux` command.

The power law model provides a statistically-acceptable fit to most of the spectra examined (§3.2.3). For these spectra, the average value of the quantity $(\Delta F/F)\sqrt{N} \sim 1.7 \pm 0.3$; where F is the intrinsic flux, ΔF its uncertainty, and N the number of source counts. For spectra poorly fit using an absorbed power law, the intrinsic flux was estimated using the `flux` command applied to the best-fitting model with the model absorption component temporarily set to zero and the uncertainty was estimated as $\Delta F = 1.7(F/\sqrt{N})$.

2.3.3. Temporal Analysis

From the time series of events within the source extraction regions, the X-ray light curves were grouped into

⁵ <http://asc.harvard.edu/ciao2.1/downloads/scripts/destreak.ps>

⁶ <http://www.astro.psu.edu/users/chartas/xcontdir/xcont.html>

1000-s bins and χ^2 tests performed against the constant count rate hypothesis to test for source variability. The Kolmogorov-Smirnov (K-S) statistic was also computed to test the sources for time variability by comparing the cumulative event arrival times, binned at the nominal frame time (3.24 s in full-frame mode), to that expected for a steady source.

For the subset of variable sources, as deduced from either of these two tests, power density spectra (PDS) were also examined. Using the Leahy normalization (Leahy et al. 1983), the average power is 2.0 (as expected from Poisson noise) and fluctuations up to 10–15 are commonly seen with a maximum power in one or two frequency bins typically between 15 and 20 in the normalized power spectra. Fluctuations of this order are due to noise. No values above these levels were observed. Therefore, no statistically-significant periodicities were obtained from analysis of the power spectra.

2.3.4. Spatial Analysis

The data were checked to ensure the nominal pointing accuracy⁷ using the latest alignment files (c. 2002 May 02). The accuracy of absolute positions in the *Chandra* data have a typical rms radius of 0.''6 (Aldcroft et al. 2000). Refinements to absolute positions conceivably can be made by cross-correlating X-ray positions with available astrometric catalogues. However, this has proved impractical for the following reasons: (1) By design, analysis is restricted to the small, source-crowded, areas of the sky within the host galaxy's D_{25} . (2) The sample of galaxies are typically far from the Galactic plane where field stars are relatively rare.

Refined estimates of the centroids of the sources were made by fitting an elliptical Gaussian to the spatial distribution of X-ray events. This method works well for locating the centroids of the model *Chandra* point spread functions, at various off-axis angles and (monochromatic) energies, available from the *Chandra* X-ray Center PSF library⁸. For ULX candidates (those with of order 100 c or higher), we estimate the statistical uncertainty in the source positions due to centroiding errors is less than 0.''1. Source celestial positions quoted in this work are these centroid-refined positions.

Radial profiles were extracted from a subset of sources and compared to model PSFs available from the *Chandra* X-ray Center. The subset of sources was chosen as those with >10% of X-ray events within the source extraction region attributable to background. As the background region encircles and is contiguous with the source region, sources with high background are either embedded in diffuse emission (a true background) or are extended. Where other sources were nearby, these were deleted from the data prior to extracting the radial profile. No ULX candidate appeared significantly extended according to this comparison.

3. RESULTS

The resulting sample of galaxies and some of their properties (distance, L_B , L_{FIR} , and nearest-neighbor distance θ_p) are listed in Table 1. Also included is a log of the corresponding *Chandra* observations. In a few cases,

two *Chandra* observations of a single galaxy were combined to increase the signal-to-noise but each observation is listed separately in Table 1. The observation log includes the fraction, f_{FOV} , of the angular size defined by the D_{25} ellipse falling within the instrument field of view; an estimate, L_{min} , of the luminosity of the weakest source for which a statistically-meaningful spectral fit could be made; and citations to previous analysis of the X-ray data from the literature. Observations performed in sub-array mode are noted in the f_{FOV} column of Table 1. The tabulated luminosity, L_{min} , corresponds to roughly 50 source counts. The source *detection* limit is about 10 c.

3.1. The Sample of Galaxies

The distribution of galaxies in the *Chandra* sample over Hubble morphological type is shown in Figure 1. There are 18 elliptical galaxies, 9 lenticulars, 46 spirals, and 9 irregulars and peculiars for a total of 82 galaxies. Typically, in this work, galaxies earlier than S0/a are collectively referred to as ellipticals and the remainder as spirals. While the full range of morphological types is represented in the *Chandra* sample, the 1:2 ratio of ellipticals-to-spirals is higher than the ratio 1:4 in the Tully (1988) Nearby Galaxy Catalogue and the $\sim 1:3$ ratio in the RC3.

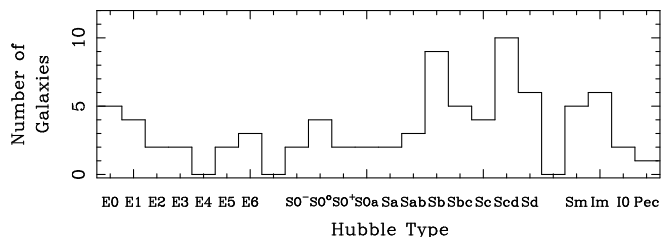


FIG. 1.— Distribution of Hubble morphological types among the *Chandra* sample of galaxies.

The *Chandra* sample of galaxies is not expected to be complete to any specified limiting distance, magnitude, or other property. However, the *Chandra* sample can be compared to, for example, the Tully (1988) Nearby Galaxy Catalogue of 2367 galaxies. The distribution of absolute blue magnitudes of the *Chandra* sample of galaxies is compared in Figure 2 to those of the 1768 galaxies in the Tully catalogue with tabulated absolute blue magnitudes. The average of the *Chandra* sample is 0.8 mag brighter in blue light than is the Tully sample. The distributions of galaxy distances for the *Chandra* sample and for the Tully catalogue are shown in Figure 3. The average distance of galaxies in the *Chandra* sample is 11.5 ± 1.2 Mpc compared to 22.5 ± 0.4 Mpc for the Tully galaxies. Similarly, the D_{25} angular sizes are larger for the *Chandra* sample (average $8.''2 \pm 0.''8$) compared to the Tully galaxies ($3.''8 \pm 0.''5$). Thus, the *Chandra* sample is comprised of nearby galaxies of large angular size and high blue luminosity compared to the Tully catalogue of galaxies. The sample is also expected to be more luminous in X-ray light as X-ray luminosity correlates with blue luminosity (e.g., Fabbiano & Trinchieri 1985; Fabbiano 1989) though the correlation varies with morphological type and is nonlinear (Fabbiano & Shapley 2002). The departure of the *Chandra* sample from

⁷ http://asc.harvard.edu/cal/ASPECT/fix_offset/fix_offset.cgi

⁸ ftp://cda.harvard.edu/pub/arcftp/caldb/axis_psflib.2.9.tar

the Tully catalogue is not unexpected as the *Chandra* sample represents an X-ray-selected sample.

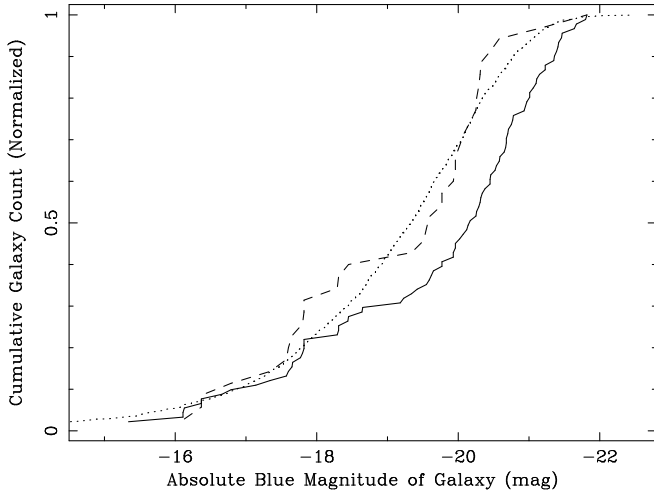


FIG. 2.— Cumulative distribution of the *Chandra* sample of galaxies (solid curve) compared to galaxies from the Tully (1988) catalogue (dotted) over absolute blue luminosity. Also shown (dashed) is the cumulative distribution of a subsample of the *Chandra* galaxies having the same distribution of absolute blue luminosity as the Tully catalogue.

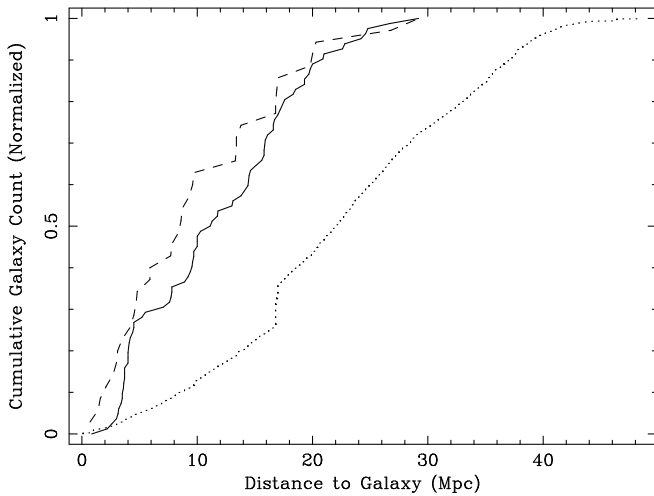


FIG. 3.— Cumulative distribution of the *Chandra* sample (solid curve) and subsample (dashed, see text) of galaxies compared to galaxies from the Tully (1988) catalogue (dotted) over distance.

In order to further assess the extent of any selection bias in the *Chandra* sample, a subsample of galaxies having the same distribution of absolute *B* magnitudes as Tully-catalogued galaxies within $D=29$ Mpc was selected. In § 3.3, this subset is used along with the full *Chandra* sample of galaxies to study correlations between the ULX candidates and properties of their host galaxies. The subsample was chosen by first grouping the full sample and the Tully catalogue into 4 bins spanning $-22.5 < M_B < -14.5$ with a 2.0 mag width for each bin. (There were too few galaxies in the full *Chandra* sample to afford a smaller binsize.) The subsample was then constructed by randomly selecting galaxies from each bin such that the fraction of subsample galaxies in each bin equals the fraction of Tully galaxies in that bin. The distribution of absolute blue magnitudes and distances of

the subsample are shown in Figures 2 and 3, respectively. The average subsample galaxy distance is 10.2 Mpc and the average D_{25} angular size is $9''.3$. The Tully catalogue of galaxies within 29 Mpc and with tabulated M_B average 16.4 Mpc and $4''.2$.

The $(B-V)$ colors of the *Chandra* sample all fall within the range of 0.5 to 1.0 mag. Therefore, although blue light is more sensitive to the properties of the stellar population of the host galaxy than is visible light, the blue luminosity is used here as a proxy for galaxy mass with an estimated factor of two uncertainty assuming $M_V \propto \text{mass}$. On the other hand, a galaxy's far-infrared luminosity is proportional to its recent star formation rate (Kennicutt 1998). The distribution of the sample of galaxies in blue and far-infrared luminosity is shown in Figure 4. Elliptical galaxies tend to cluster near the upper left in this figure indicative of a relatively high mass but little or no recent star formation. In contrast, spiral galaxies span from lower-left to upper-right showing a general trend of star formation rate proportional to galaxy mass. It is also evident that spirals have a higher star formation rate per unit mass (blue light) compared to the ellipticals.

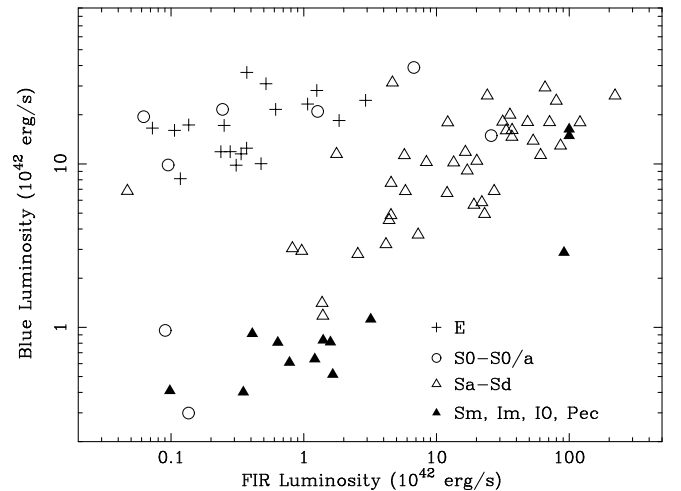


FIG. 4.— Distribution of the *Chandra* sample of galaxies in blue and far-infrared luminosity.

3.2. The ULX Candidates

Approximately 3400 X-ray sources were detected above a signal-to-noise ratio of 2.8 (resulting in >10 c per source and much less than 1 false detection per field) within the D_{25} areas of the 82 galaxies analyzed. Among these are ~ 1900 sources with intrinsic luminosities estimated from detected counts exceeding $\sim 10^{38}$ ergs s^{-1} . The source-region image, spectrum, and light curve were examined for all these sources though only 837 had sufficient counts (>50) for further analysis. Detailed spectral fits were made to 357 of these sources and 154 were determined to have luminosities in excess of 10^{39} ergs s^{-1} in the 0.5–8.0 keV energy range.

We may therefore define three source populations: (1) The 837-member group above an estimated 10^{38} ergs s^{-1} and with >50 c detected for which X-ray colors have been determined and the K-S test applied to the X-ray light curves, (2) The 357-member subset for which spectral parameters and hence luminosities have been established,

and (3) the subset of 154 ULX candidates. Table 2 lists the celestial positions and X-ray properties of the ULX candidates.

The subset of ULX candidates is complete to the extent that the derived luminosities (and hence adopted distances) are correct. The completeness level of the 357 sources with spectral fits made can be estimated as the luminosity where their cumulative luminosity function begins to flatten. This occurs at $L_X \sim 4 \times 10^{38}$ ergs s $^{-1}$ with about 20% lying below this completeness level. These lower-luminosity sources tend to be those from nearby galaxies with deep exposures but are otherwise not expected to differ from sources above the completeness limit. The lowest luminosity of a source for which spectral parameters have been established is 8.9×10^{37} ergs s $^{-1}$. The luminosities for the first group were estimated from the number of detected counts in the manner described in § 2.1 and are therefore much more uncertain than for the other two source populations. The completeness level for this population, based on its cumulative luminosity function is also $\sim 4 \times 10^{38}$ ergs s $^{-1}$. More importantly for this population, however, is that there are sufficient counts detected for analyzing their X-ray colors and timing properties without overwhelming statistical uncertainties. Thus, this population is limited to sources with >50 c detected.

3.2.1. X-ray Spectra

The 3-parameter absorbed power law model provides one of the simplest phenomenological descriptions of X-ray spectra. This model was applied to the observed spectra to constrain the observed and intrinsic luminosities of the sources (see also § 2.3.2 above) and to establish their basic spectral shapes. Statistically-acceptable ($>90\%$ confidence) fits were obtained using this model for 83% (298 of 357) of sources for which spectral parameters have been determined and for 130 (84%) of the ULX candidates. This does not imply that a power law is the only acceptable model for these spectra nor that a power law fully describes the physical mechanism(s) responsible for the observed X-ray emission. Indeed, an absorbed thermal emission line (**mekal**) model, for example, results in an acceptable fit to $\sim 78\%$ of the sources analyzed.

The fitted power law indices of the ULX candidates with statistically-acceptable power-law fits are compared in Figure 5 to the weaker sources. Overall, the distributions are very similar and can be described by the same Gaussian shape. However, there is a significant population of sources (20 of 130) with $\Gamma \gtrsim 3$ in the ULX population that does not have a counterpart in the sample of weaker sources (7 of 168).

Closer inspection showed that sources with a steep power law index often also required a high absorbing column density that compensates for an observed spectral rollover toward low energies. The average column density is $N_H/10^{20} = 38.7 \pm 3.0$ for ULX candidates with $\Gamma > 3$ compared to 19.6 ± 1.2 for the $\Gamma \leq 3$ sources. The ultimate effect is to promote steep power law sources with low *observed* luminosities into the high *intrinsic* luminosity ULX candidate category. In contrast, thermal models such as the **mekal** model have a natural rollover at low energies, do not require as large an absorbing column density, and result in a lower intrinsic luminosity.

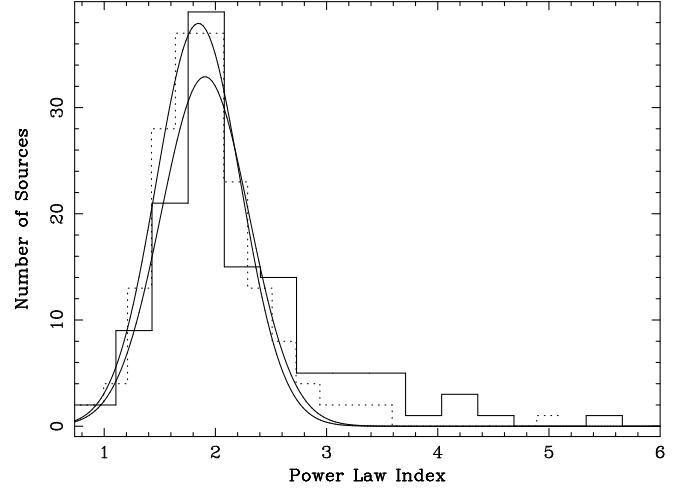


FIG. 5.— Number of ULX candidates (solid histogram) and non-ULX sources for which spectral fits were made (dotted) against power law index. The two distributions include only sources for which an absorbed power law model provides an acceptable fit. Both distributions can be described by a Gaussian with the same fit parameters within errors (centroids 1.97 ± 0.11 and 1.88 ± 0.06 for the ULXs and the other sources, respectively, and widths 0.50 ± 0.10 and 0.41 ± 0.05). The population of ULX candidates with power-law index $\Gamma > 3$ is discussed in the text.

This trend is illustrated in the upper panel of Figure 6 where the ratio of the intrinsic luminosity derived using the **mekal** model to that derived using the power law model is shown against the power law index. Only a subset of ULX candidates are included in this figure: A sample with >500 detected counts and $\Gamma < 3$ and all of the $\Gamma > 3$ sources though, in both domains, only sources with statistically-acceptable fits from both the power law and the **mekal** model are included. The difference in derived intrinsic luminosities increases rapidly with increasing Γ . For the bulk of the sources modeled (those with $\Gamma \sim 1.8$) however, both the **mekal** and power law models result in very similar intrinsic luminosities.

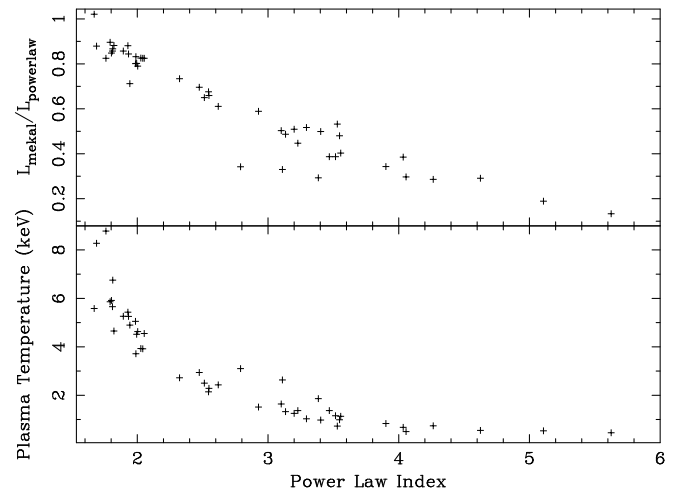


FIG. 6.— (Upper panel) Ratio of the intrinsic luminosity derived using the **mekal** model to that derived using the power law model is shown against the power law index. The power law model predicts a higher intrinsic luminosity compared to the **mekal** model with the difference systematically increasing with power law index. (Lower panel) Corresponding **mekal** model plasma temperature decreases with increasing Γ .

This systematic effect helps explain the high- Γ tail apparent in the ULX candidate population of Figure 5 but lacking in the lower luminosity source population. Applying the `mekal` model to the 20 ULX and 7 non-ULX sources with $\Gamma > 3$ and acceptable power law fits resulted in `mekal`-derived intrinsic luminosities $< 10^{39}$ ergs s $^{-1}$ for 17 of the 27 sources. These 17 are denoted in Table 2. Thus, adopting the `mekal` luminosities would result in similar high- Γ distributions for both populations. The lack, at the outset, of steep power law sources in the non-ULX population is due to the relatively low number of counts in the 0.5–8.0 keV band for this spectral shape combined with the fact that low-count sources were not selected for spectral analysis. However, the X-ray color analysis of § 3.2.2 shows that there are sources with colors equivalent to a steep power law in the low-count population.

It is evident that more than one spectral model often provides statistically-acceptable fits to the observed X-ray spectra. Often these models ostensibly represent quite different physical emission mechanisms. For example, physical models of X-ray phenomena that predict “soft” X-radiation, corresponding to a steep power law index, are cool thermal emission sources (lower panel, Figure 6), such as supernovae, while phenomena that can be characterized as non-thermal, such as synchrotron emission from a power-law distribution of electrons or Comptonization, tend to result in relatively flat power law indices. Thus, while either model is statistically-acceptable, it is reasonable to *assume* that the majority of the steep power law sources are thermal sources. Many of these may be supernovae though three $\Gamma > 3$ sources are among the most variable X-ray sources in the ULX sample (Table 2 and § 3.2.3). One of these is a known super-soft source in NGC 5457 (Mukai et al. 2003).

Having established that both the power law and the `mekal` models predict similar luminosities for the majority of sources (those near $\Gamma \sim 1.8$) and that both models effectively discriminate between “soft” and “hard” X-ray spectra, it remains to choose one or both models (or some other) as a baseline. The power law is arguably the easier to grasp conceptually and requires the fewest number of parameters. Therefore, the absorbed power law model fit parameters and derived luminosities are reported in Table 2 whenever this model provided a statistically-acceptable fit. Additional models applied to sources not well-fit by an absorbed power law were thermal emission line models (`mekal` or `vmekal`), disk blackbody models (`diskbb`) and combinations of these three (including power law) basic spectral models. Of the 24 ULX candidates poorly fit by the absorbed power-law model, 11 were acceptably-fit using 1- or 2-component thermal emission line models, 9 using disk blackbody models, and 4 were not well-fit by any of the trial spectral models. Parameters for these models are reported in Table 2 (the power law parameters are quoted for the 4 spectra with no acceptable fits).

Figure 7 shows the value of the power law spectral index, Γ , against the number of detected source counts and Figure 8 displays Γ against the derived intrinsic source luminosity. Not surprisingly, sources for which the simple absorbed power law model was unacceptable tend to be those sources with a high number of detected counts (e.g., a power law is unacceptable for 39% of the 51 sources

with >1000 detected counts compared to only 8% of 177 sources with <200 detected counts).

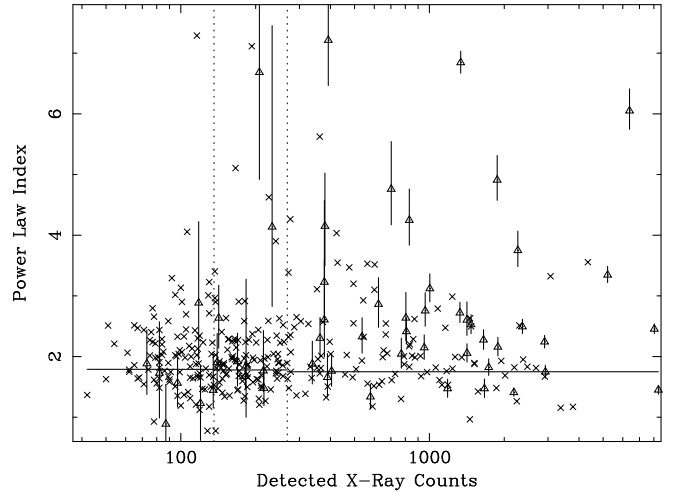


FIG. 7.— Results of simple absorbed power law model fits. Sources for which this model provides a statistically-acceptable fit at the 90% confidence level are marked with an \times and those unacceptably-fit by a simple power law are denoted by triangles. Errors shown are extremes on the single interesting parameter 90% confidence intervals. They indicate typical values for all sources with power law models applied but are not displayed for sources with acceptable fits for clarity. Formal errors for the ULX candidates are provided in Table 2. Horizontal lines denote the average power law index, for sources with an acceptable fit, on domains spanning an equal number of sources. For clarity, these domains are separated by dotted vertical lines.

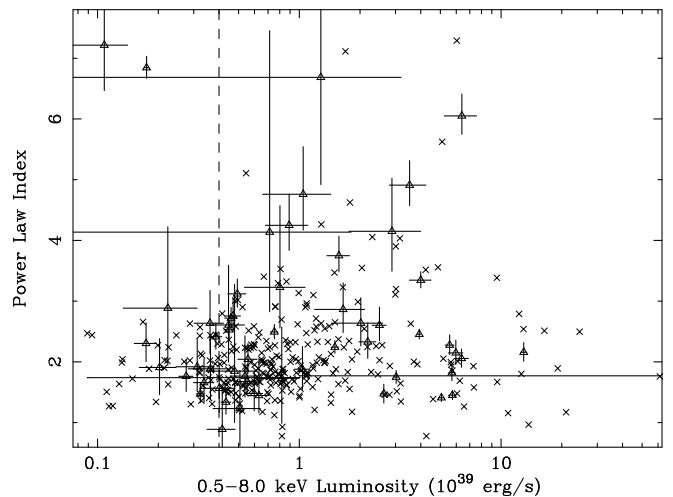


FIG. 8.— Results of simple absorbed power law model fits. Symbols are the same as in Figure 7. Note sources poorly-fit with a power law are uncorrelated with intrinsic luminosity and that many of the highest luminosity sources are well-fit with this simple model. Horizontal lines denote the average power law index, for sources with an acceptable fit, for ULX and for weaker sources. The vertical line denotes the estimated completeness limit of the sample of sources for which spectral modeling has been performed.

The average value of the power law index, $\langle \Gamma \rangle$, for sources with statistically-acceptable power law fits, are 1.79 ± 0.09 (for sources with <137 c), 1.78 ± 0.07 (137 to 268 c), and 1.75 ± 0.03 (>268 c) where the 3 ranges were chosen to contain equal numbers of sources. Similarly,

$\langle\Gamma\rangle$ is displayed in Figure 8 for the ULX candidates (1.74 ± 0.03), and for the weaker sources (1.77 ± 0.04 above the completeness limit and 1.76 ± 0.10 for sources below 4×10^{38} ergs s $^{-1}$). The dispersion of Γ about the mean value is $\sigma=1.18$ for the ULX candidates and 0.43 for the non-ULX sources. The steep power law sources account for the larger dispersion in the ULX candidates population. Restricting the range to $\Gamma<3$ results in $\sigma=0.51$ and 0.40 for the two groups. The average power law index is therefore independent of the number of detected counts and of the intrinsic luminosities of the source above our completeness limit of $\sim4\times10^{38}$ ergs s $^{-1}$. *Chandra* studies of the nearby galaxies, e.g., M31 (Kong et al. 2002) and M81 (Swartz et al. 2003), conclude that this trend continues ($\langle\Gamma\rangle\sim1.8$) even for sources as weak as 3.4×10^{37} ergs s $^{-1}$ and 2×10^{37} ergs s $^{-1}$, respectively.

3.2.2. X-ray Colors

There are many more weak sources detected than can be meaningfully analyzed through spectral fitting. A common tool used for low-count sources and low-resolution spectra is the X-ray color-color diagram. Prestwich et al. (2003) advocate $(H-M)/(H+M+S)$ and $(M-S)/(H+M+S)$ as colors that provide some physical insight into the nature of X-ray source populations and these colors are adopted here.

The X-ray colors of the 154 ULX candidates and of the 837 sources with estimated luminosities above 10^{38} ergs s $^{-1}$ and >50 c are shown in Figures 9 and 10, respectively. Error bars, propagated from the statistical uncertainties in the three X-ray bands, are omitted from Figure 10 for clarity. Colors of absorbed power law model spectra (for sources imaged on back-illuminated CCDs) are also shown for reference as solid curves. The front-illuminated devices have relatively lower response in the soft band so that similar curves for these devices do not extend to such low values of $(M-S)/T$. Nevertheless, the differences are typically much less than the uncertainties in the X-ray colors.

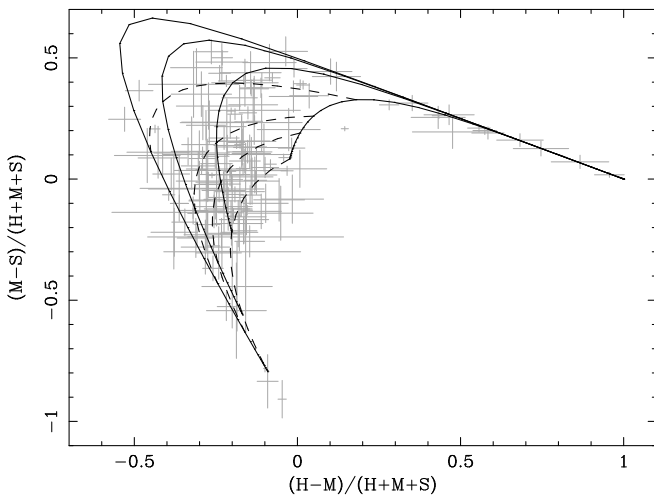


FIG. 9.— X-ray colors of the ULX candidates. Solid curves denote colors of absorbed power law models of spectral indices $\Gamma = 1, 2, 3$, and 4 (from right to left) and for the range of absorbing columns $n_H = 10^{20}$ to 10^{24} cm $^{-2}$. Dashed curves denote constant absorption columns of $n_H = 10^{20}$, 10^{21} , 2×10^{21} , and 5×10^{21} cm $^{-2}$ (from bottom to top). Errors shown were propagated from the statistical uncertainties in the three X-ray bands.

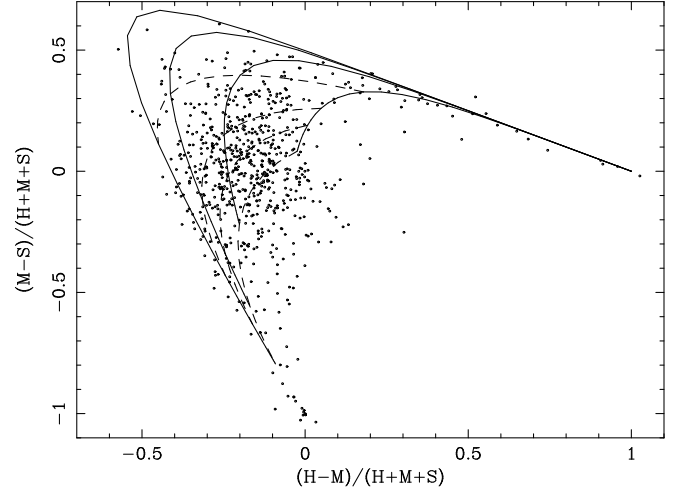


FIG. 10.— X-ray colors of sources with luminosities, estimated from observed counts, in excess of 10^{38} ergs s $^{-1}$ and detected counts >50 . Curves same as Figure 9. Errors omitted for clarity.

Highly-absorbed sources lie near (1,0) and super-soft sources near (0,-1) in these figures. The colors of steep power law sources are constrained along a narrow band extending from the super-soft source location at (0,-1) upwards and to the left towards $\sim(-0.6,0.5)$. The region to the left of this band is physically inaccessible (curves of constant Γ converge rapidly as Γ increases as shown in the figures). According to Prestwich et al. (2003), the sources in the region centered at about (-0.2,0.0) are predominately low-mass X-ray binaries and are common to both spiral and elliptical galaxies.

Visually, the two color distributions appear similar. Applying a two-dimensional Kolmogorov-Smirnov test (Peacock 1983; Fasano & Franceschini 1987) to the color-color distributions of the ULX candidates and of *all* 1900 sources with luminosities above 10^{38} ergs s $^{-1}$ resulted in a significance level of $P_{KS} = 0.01$. However, the Kolmogorov-Smirnov test does not account for (statistical) uncertainties in the data. When the test was applied to the restricted set of sources with >50 detected counts (those depicted in Figures 9 and 10), the significance level increased to $P_{KS} = 0.17$, showing that the distributions are marginally consistent with being from the same parent population.

3.2.3. X-ray Timing

The Kolmogorov-Smirnov probability, P_{KS} , that a source is constant was computed for the population of sources with estimated luminosities exceeding 10^{38} ergs s $^{-1}$ and for the subset of ULX candidates. Analysis was limited to those sources with >50 detected counts as variability is more easily detected at higher signal-to-noise.

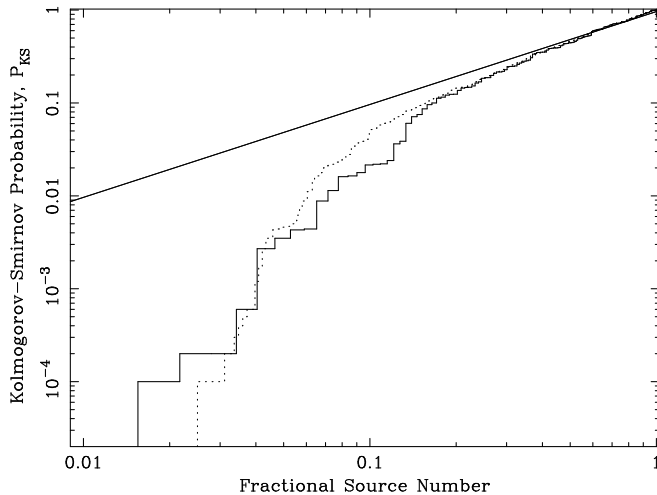


FIG. 11.— Results of a Kolmogorov-Smirnov test of the hypothesis that the distribution of photon arrival times for X-ray sources is equivalent to that of a source with constant flux. Shown is the value of the significance level, P_{KS} , for each source with estimated luminosity exceeding 10^{38} ergs s^{-1} and >50 detected counts (*dotted*) and for the ULX candidates (*solid*) ordered by increasing values of P_{KS} . The line has slope unity. The abscissa is scaled by the inverse of the number of sources in the two populations ($1/837$ and $1/154$, respectively).

Figure 11 displays the distribution of these probabilities for the two populations. The line denotes the linear trend of the data. For purposes of discussion, we may consider sources with $P_{KS} \lesssim 0.001$ as significantly variable and those with $P_{KS} \lesssim 0.04$, the point where the slope of the curve changes noticeably, as likely to be variable. There are 80 sources (9.6%) with $P_{KS} < 0.04$ and 33 (3.9%) with $P_{KS} < 0.001$ for the larger sample. If the ULX candidate population had the same distribution, then 15 and 6 ULXs, respectively, would be expected to lie below these values of P_{KS} . For the ULX candidates, there are 22 and 7 sources, or 14.3% and 4.5%, respectively, below these two benchmarks. This is within statistical errors of the expected values. Of particular importance is the fact that the photon arrival times for 86% of the ULX candidates are consistent with the constant flux hypothesis.

Note that the ULXs tend to be those with higher numbers of counts so that variability is more easily discerned with this test in this population. The K-S test is sensitive to long term variability even when the data has been finely binned. This is in contrast to other methods which often have an optimal binning typically of the same order as the variability timescale under consideration. Simulations were run to estimate this sensitivity. Consider the function $R(1 + M\sin(2\pi t/P))$, where R is the average count rate, M is the modulation amplitude, and P is the period. Events were randomly generated in each timebin with a Poisson distribution with the mean given by the function. For 5000 bins and $R = 0.02$ c bin^{-1} , the simulation will generate about 100 c. For this case and a period of 5000 bins, M needs to be about 0.35 in order for the K-S probability to be 10%. In other words, if the modulation is 35% and the K-S threshold is 10% then about half the time the K-S probability will be less than 10% and the variability “detected”. If P is 2500,

then the amplitude needs to be 0.60 and for P of 1500 an amplitude of 1.00 only results in a K-S probability of 15%. As expected the amplitude scales roughly as $N^{-1/2}$, where N is the number of counts.

As displayed in Figure 11, the distributions are themselves cumulative distribution functions and applying the Kolmogorov-Smirnov test to compare these two distributions shows that they are consistent with being drawn from the same distribution ($P_{KS} = 0.95$).

3.2.4. X-ray Source Locations

The relative radial position of each X-ray source can be expressed as the fraction, f , of the deprojected galaxy radius in units of $1/2$ the D_{25} diameter. Figure 12 shows the resulting surface distribution of all 3413 discrete X-ray sources detected in the survey, of all ULX candidates, of ULXs in spiral galaxies, and of ULXs in ellipticals. Recall that sources within $5''$ of the galaxy centers have been excluded from consideration as ULXs.

The distributions can be approximated by a generalized exponential function (plus a constant) of the form $A \exp^{-(f/h)^{(1/n)}}$ where h is a scale height and n is the index. The distributions of all detected sources and of all ULX candidates can be approximated by the same values of scale height ($h = 0.06 \pm 0.03$) and index ($n = 1.59 \pm 0.32$, where the quoted errors are for the larger population of all detected sources, $\chi^2 = 105.9$ for 93 dof and 25.1 for 17 dof, respectively). Fits to the smaller subsets of spirals or ellipticals give large ranges to the fit parameter values when all parameters are allowed to vary. If n is held to the best-fit value of 1.59, then the values of the scale heights are within the uncertainties, $h = 0.06 \pm 0.04$ ($\chi^2 = 19.9$ for 16 dof) for the spirals and $h = 0.04 \pm 0.02$ ($\chi^2 = 21.4$ for 15 dof) for ellipticals.

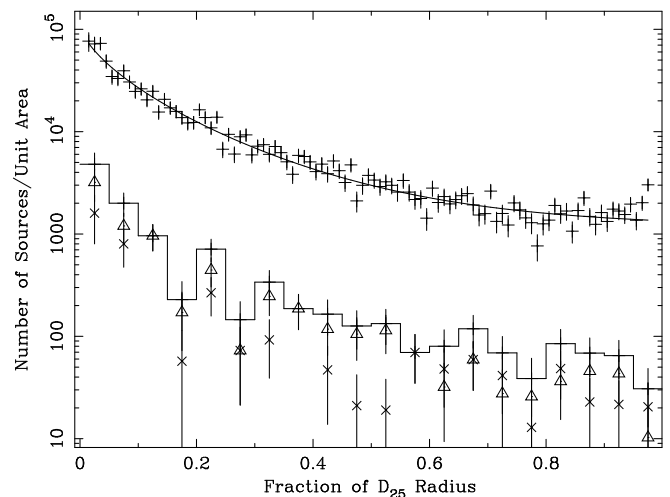


FIG. 12.— Surface distribution of all X-ray sources detected in the sample (*top*) and of the subset of ULX candidates (*bottom*, full curve). ULX candidates in spiral galaxies are marked with triangles and those in elliptical galaxies with \times 's. The abscissa is the deprojected radial position, f , expressed as a fraction of the host galaxy's angular radius ($\equiv 0.5D_{25}$) and the ordinate is the number of sources per unit area, $f df$, on the range f to $f + df$. The curve drawn through the upper dataset is the best-fit generalized exponential function described in the text.

Fitting a constant to the surface density distributions of the ULX populations in ellipticals and spirals results in

an acceptable fit for ellipticals but not for spirals. For ellipticals, the value of the constant is 29.1 ± 9.1 , $\chi^2 = 23.3$ for 17 dof, on the entire domain. On the restricted domain, $f > 0.1$, where the distribution appears to flatten (Figure 12), the value is 28.8 ± 9.1 , $\chi^2 = 13.9$ for 15 dof. For spirals, $\chi^2 = 63.7$ for 18 dof and $\chi^2 = 47.4$ for 16 dof in these two domains, respectively. Thus, the ULX candidates have the same spatial distribution, statistically, as does the larger population of all detected sources but the spatial distribution of ULX candidates in ellipticals is much flatter than for spirals with the exception of a few sources near the centers.

3.2.5. Estimated Contribution from Background Sources

The detection limit for discrete sources is about 3×10^{-15} ergs cm $^{-2}$ s $^{-1}$, for the average exposure time of 39.6 ks, and the total area of the sky covered by the survey is 0.9 deg $^{-2}$. Comparing this to the *Chandra* Deep Field (CDF) results of Brandt et al. (2001) and of Rosati et al. (2002), we expect about 1100 of the 3400 detected sources are background (consistent with the value of the constant term, 1144 ± 215 , in the surface distribution model described in §3.2.4). This corresponds to ~ 12 background sources per galaxy given the average galaxy area is 36.2 min 2 .

The results for the ULX candidates, however, are based on luminosities and not fluxes. Thus, a straightforward comparison to the CDF results is not possible. Instead, in Figure 13, is shown the $\log(N(> S)) - \log(S)$ distributions of ULX candidates for each galaxy, where S is the observed flux and $N(> S)$ is the number of sources with flux $> S$ and scaled by the area of the galaxy within the instrumental field of view in units of deg $^{-2}$. Also shown is a curve, $N(> S) = 16(S/10^{-13})^{-1.7}$, representing the high-flux $\log(N(> S)) - \log(S)$ results of the ASCA Large Sky Survey (Ueda et al. 1998) and Deep Sky Survey (Ogasaka et al. 1998) and the low-flux results from Brandt et al. (2001). Points near or below this curve are likely background objects and not true ULXs. The number of background sources can be estimated as follows. If the flux from the weakest ULX candidate in a galaxy (of area A deg 2) is denoted S , then we expect a contribution of at most $16(S/10^{-13})^{-1.7}A$ to the number of background sources from that galaxy field. If the slope of the galaxy's $\log(N(> S)) - \log(S)$ distribution is flatter than $S^{-1.7}$, then this is an overestimate. The sum of such contributions from all galaxies gives a conservative estimate of 39 background sources among the 154 ULX candidates, or 25%.

Note that the distribution depicted in Figure 13 suggests many ULX candidates in elliptical galaxies are more likely to be background sources than those in spiral galaxies. Using the method outlined above yields an estimate of 25 background sources, or 44%, among the elliptical galaxy ULX candidates while only 14 sources (14%) of the ULX candidates in spirals are potentially background objects. This result is consistent with the sample of elliptical galaxies analyzed by Irwin et al. (2003). However, there are several ULXs in our sample of elliptical galaxies that do not follow this trend.

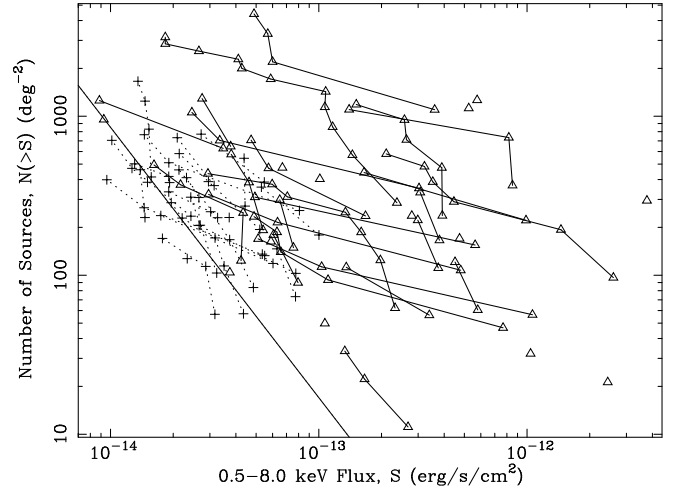


FIG. 13.— $\log(N(> S)) - \log(S)$ distribution for ULX candidates. The ordinate is the number of ULX candidates identified in each galaxy above a given flux scaled by the angular size of that galaxy. Spiral galaxies are denoted by triangles and solid lines. Ellipticals are denoted by crosses and dotted lines. The power law curve denotes an approximate fit to the point-source X-ray background (e.g., Brandt et al. 2001), scaled to our bandpass (0.5–8.0 keV), and is given by $N(> S) = 16(S/10^{-13})^{-1.7}$. Note several galaxies host only one ULX candidate.

3.2.6. X-ray Luminosity Function

The cumulative luminosity functions (XLFs) of the ULX candidates in elliptical and in spiral host galaxies are displayed in Figure 14. There are 57 ULX candidates in the 27 elliptical galaxies and 97 in the 55 spiral galaxies. While the number per galaxy are roughly equal, ULXs in spiral galaxies are much more luminous. Two-thirds of the ULXs in spiral galaxies are above 2×10^{39} ergs s $^{-1}$ while only 1/3 of ULXs in ellipticals are this luminous.

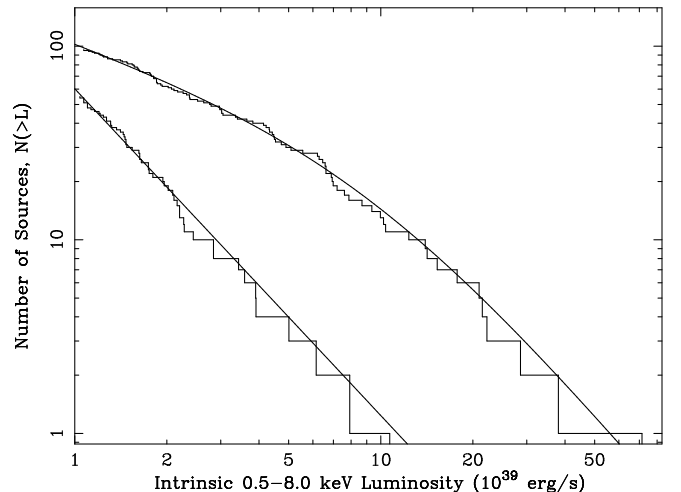


FIG. 14.— Cumulative luminosity function of ULX candidates in spiral (upper curve) and in elliptical galaxies. A power law with slope -1.72 ± 0.14 describes the luminosity function for ellipticals. A broken power law model is shown for spirals. (A power law with an exponential cut-off also provides an acceptable fit for spirals though a single power law does not.) The slope is -0.56 ± 0.05 at low luminosity and the break luminosity is $\sim 10 \times 10^{39}$ ergs s $^{-1}$.

Using a maximum-likelihood statistic, a power law adequately describes the luminosity function for elliptical

cals with a slope -1.72 ± 0.14 . More complex models do not improve the fit significantly. A broken power law (change in statistic $\Delta C = 26.7$ compared to a simple power law) or a power law with an exponential cut-off ($\Delta C = 23.8$) is needed to describe the luminosity function for spirals. The slope of the broken power law is -0.56 ± 0.05 at low luminosity, the break luminosity is 9.6 ± 0.6 in units of 10^{39} ergs s^{-1} , and the slope at high luminosity is -1.88 ± 0.30 . The slope of the cut-off power law model is -0.64 ± 0.09 with a cut-off luminosity of $(19.4 \pm 8.6) \times 10^{39}$ ergs s^{-1} .

3.3. ULXs and their Host Galaxies

Several global properties of the host galaxies are available as described in § 2.2. Linear correlation coefficients were computed for various paired combinations of the following quantities compiled for each galaxy: number of ULXs (N_{ULX}); total X-ray luminosity from ULXs (L_{ULX}); average ULX luminosity (L_{ULX}/N_{ULX}); blue luminosity (L_B), far-infrared luminosity (L_{FIR}), nearest-neighbor distance (θ_p), and D_{25} area. Linear correlation coefficients for the most significant correlations are listed in Table 3. In addition to the entire sample of galaxies, coefficients were computed for the subsets of elliptical and of spiral galaxies and for the subsample of *Chandra* galaxies with the same distribution of absolute B magnitudes as the Tully catalogue of galaxies (see § 3.1).

The strongest correlations for elliptical galaxies are between ULX properties and the host galaxy's L_B , while those for spirals are with L_{FIR} and a marginally-significant correlation with θ_p . There are no significant correlations for the subsample of elliptical galaxies. The subsample of spiral galaxies again correlate with L_{FIR} but also with L_B . The subsample of galaxies was designed to minimize some of the biases in the full sample. Although the subsample contains only 34 galaxies, the significance of the correlations between ULX properties and L_{FIR} for spirals remains strong enough to show this result is robust.

While there are ~ 2 ULX candidates per galaxy for both ellipticals and spirals (§3.2.6), the number per unit (10^{42} ergs s^{-1}) blue luminosity for ellipticals is only 0.11 ± 0.02 compared to 0.30 ± 0.11 for spirals. The total ULX luminosity, L_{ULX} , per unit L_B is 0.19 ± 0.05 for ellipticals and 1.63 ± 0.88 for spirals. Therefore, the pairs of parameters were again examined after first normalizing to unit L_B . No significant changes in the correlation coefficients occurred though the correlations between ULX properties and L_{FIR} increased for spiral galaxies.

The correlation between the number of ULX candidates and L_{FIR} is displayed in Figure 15 for the spirals and ellipticals. For spirals, the linear relation between the two is $N_{ULX} = (0.022 \pm 0.01)L_{FIR}/10^{42} + (0.64 \pm 0.3)$. Note that the highest L_{FIR} bin is dominated by the Antennae pair of galaxies with 13 ULX candidates. On the other hand, the spiral galaxies with $L_{FIR} \lesssim 4 \times 10^{42}$ ergs s^{-1} are the dwarf irregulars (cf. Figure 4). For ellipticals, the strongest correlation is between the number of ULXs and blue luminosity and is given by $N_{ULX} = (0.095 \pm 0.05)L_B/10^{42} + (-0.11 \pm 0.7)$.

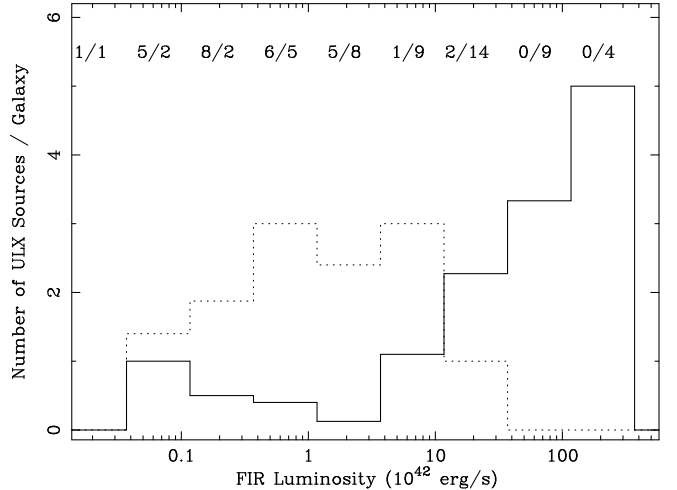


FIG. 15.— Number of ULX candidates per galaxy is shown against the host galaxy's far-infrared luminosity. For spiral galaxies (solid histogram), the correlation is significant (Pearson's linear correlation coefficient $r = 0.88$) but not for ellipticals (dotted, $r = 0.15$). The numbers of elliptical/spiral galaxies within each L_{FIR} bin are displayed across the top of the figure.

4. DISCUSSION

We have presented the spectrophotometric X-ray properties of a population of 154 ULX candidates taken from a sample of 82 galaxies observed with *Chandra*. We have shown that ULXs are more numerous and luminous in galaxies with indications of recent star formation as measured by their far-infrared luminosities and by their morphologies (Hubble type and, less significantly, nearest neighbor distance). We have also compared the ULX candidates with the less-luminous X-ray sources in the same galaxy fields and found their X-ray properties statistically indistinguishable.

4.1. ULXs and Less-Luminous Sources

The similarity between ULX candidates and the less-luminous population exists among all observable X-ray properties: spectral shapes, colors, time series, and (radial) positions within their host galaxies. This result has two important implications. First, as the less-luminous population is a composite of low- and high-mass X-ray binaries and supernova remnants (to our formal detection limit but also must include some foreground objects such as cataclysmic variables and stellar coronae as well as background AGNs); our results imply the ULX candidates are also a heterogeneous group of objects. Secondly, the similar distributions of physical characteristics suggests, as the simplest explanation, that ULXs may be the high-luminosity end of a continuous distribution of supernova remnants and accreting systems such as X-ray binaries.

These conclusions do not diminish the fact that ULXs retain their distinction as the most luminous non-nuclear X-ray sources. How are such high luminosities achieved? Contemporary explanations for the ULX phenomenon fall into three broad categories; massive accreting objects, anisotropically-emitting sources, and supernovae. As part of their appeal, each of these models effectively circumvent the benchmark Eddington limit luminosity, $L \sim 1.4 \times 10^{38} (M/M_{\odot})$ ergs s^{-1} , that expresses the balance between the inward force of accreting material against

the outward radiation force. X-ray binaries with compact object masses $>100 M_{\odot}$ raise the Eddington limit to $>10^{40}$ ergs s^{-1} . Anisotropically-emitting X-ray binaries avoid the Eddington limit in two ways: The emission may be in a direction other than opposing accretion and, secondly, the actual luminosity is less than the apparent (assumed isotropic) luminosity by a factor $b = \Omega/4\pi$ where Ω is the solid angle of emission. For accreting sources, it is also necessary to attain an accretion rate, $\dot{M} \gtrsim 10^{-6} b M_{\odot} \text{ yr}^{-1}$, as the apparent luminosity scales as $\sim 6 \times 10^{45} \dot{M}/b$ ergs s^{-1} [and so the slim-disk scenario that applies at high accretion rates (Abramowicz et al. 1988; Watarai et al. 2001; Ebisawa et al. 2003) may be favored over standard thin-disk models]. The third category, supernovae, are, of course, not Eddington limited in the first place. Each of these scenarios predict different observable X-ray properties which can be compared to our results.

4.1.1. *Intermediate-Mass Black Holes*

Colbert & Mushotzky (1999; see also Makishima et al. 2000; Colbert & Ptak 2002) suggest that ULXs are accreting black holes (BHs) with masses intermediate between stellar mass ($\lesssim 20 M_{\odot}$) and supermassive objects (active galactic nuclei, 10^6 to $10^9 M_{\odot}$). This is perhaps the most intriguing scenario because it suggests a possible observable link between stellar collapse and the formation of active galactic nuclei (see van der Marel 2004; Miller & Colbert 2003 for reviews). Fryer & Kalogera (2001) show, however, that single stars in the current epoch rarely form BHs with masses $\gtrsim 15 M_{\odot}$. First-generation, zero-metallicity (Population III) stars, on the other hand, were on average more massive than today's population, would have retained more mass as they evolved because of inefficient wind mass loss, and may have left more massive BH remnants. Intermediate mass black holes (IMBHs) may also form in dense young star clusters through runaway merging of massive stars (Ebisuzaki et al. 2001; Portegies Zwart & McMillian 2002; Portegies Zwart et al. 2004) or through the gradual accretion of compact stellar remnants onto a seed black hole over the lifetime of the cluster (Miller & Hamilton 2002).

In analogy to stellar-mass black hole X-ray binaries (e.g., McClintock & Remillard 2003), the IMBH X-ray spectrum should be a power law with a soft thermal (blackbody) component with a characteristic temperature scaling as the $-1/4$ th power of the compact object mass (e.g., Makishima et al. 2000). Those ULX candidates with blackbody disk spectral shapes typically have temperatures of order 1 keV (with two exceptions which lie near (0, -1) in the color-color diagram, Figure 9, i.e., they are supersoft sources with no additional power law component). Thus, we find no prominent component at $kT \sim 0.1$ – 0.2 keV in our sample. A few ULX candidates with soft accretion disk components have been reported (e.g., Miller et al. 2003; Roberts & Colbert 2003).

To further the analogy to stellar-mass BHs, IMBHs can also be expected to display soft/hard spectral transitions. Furthermore, transient behavior is predicted by Kalogera et al. (2004) for accreting IMBH systems due to a thermal-viscous disk instability. Neither of these transitions are accessible in the short observations typi-

cal of our sample but have been reported for a few well-monitored ULXs (e.g., La Parola et al. 2001; Kubota et al. 2001).

IMBHs formed from individual Population III stars are expected to be distributed throughout the host galaxy and to be present in all galaxy types (Madau & Rees 2001). IMBHs formed in dense stellar environments should remain associated with globular clusters. They should occur frequently in elliptical galaxies as these galaxies have large numbers of globular clusters. Furthermore, the ULX spatial distribution should follow that of the halo stars in contrast to the distribution of weaker sources that follow the distribution of disk and bulge stars. These trends are difficult to discern in the current sample. The ULXs are distributed in the same way as the weaker sources (though the distribution in ellipticals is arguably flatter, §3.2.4) and the number of ULXs per galaxy is no higher in cluster-rich ellipticals compared to spirals. Note that an IMBH accretor need not be invoked for the majority of ULXs in elliptical galaxies where $2/3$ of the ULXs (§ 3.2.6) are less luminous than 2×10^{39} ergs s^{-1} and, according to Irwin, Bregman, & Athey (2004), those more luminous than 2×10^{39} ergs s^{-1} may all be background objects.

4.1.2. *Anisotropic X-ray Binaries*

There are several beaming models: One model (King et al. 2001) assumes a phase of super-Eddington accretion is present, perhaps due to thermal-timescale mass transfer, that forms a thick disk with a central funnel that results in mildly-beamed emission (see also Madau 1988). Another model envisions the formation of a jet with an enhancement of the X-radiation via Compton scattering of photons (from the accretion disk or from a high-mass companion) by relativistic electrons in the jet (Georganopoulos et al. 2002). A third model envisions direct, relativistic Doppler boosted, synchrotron emission from the (face-on) jet itself (Fabrika & Mescheryakov 2001).

The spectral signature of the beaming model has not been specified. Compton scattering from jets and direct synchrotron emission should display a characteristic steep power law spectra. If ULX emission is beamed and weaker sources are not, then one would expect the two populations to have different spectral indices. While the spectral shape of the majority of the ULX candidates are consistent with power laws, their spectral indices do not differ from the less luminous population. Large-amplitude variability is also expected from relativistic jets. The high mass transfer rates implied for the mildly beamed sources (King et al. 2001; Kalogera et al. 2004) result in stable disks and persistent X-ray emission. There are no preferred locations or galaxy type for beaming models. However, thermal-timescale mass transfer occurs when the main-sequence mass-donor (companion) star is more massive than the compact accretor. This requires an early-type companion of moderate mass, $\gtrsim 5 M_{\odot}$, and hence such systems will occur rarely in ellipticals.

4.1.3. *Energetic Supernovae*

A third scenario is an unusually energetic supernova, or hypernova (Wang 1999). Supernovae exploding in high-density environments have been hypothesized to reach

X-ray luminosities sufficient to power the broad-line regions of active galactic nuclei (Terlevich, Melnick, & Moles 1987; Terlevich et al. 1992). Supernovae have been observed with luminosities as high as $\sim 10^{40}$ ergs s $^{-1}$ months to years after their discovery (Schlegel 1995; Immler & Lewin 2003). For example, SN 1986J in NGC 891 has a luminosity of $\sim 6 \times 10^{39}$ ergs s $^{-1}$ according to our calculations (Table 2).

Supernovae display the distinct thermal emission-line X-ray spectrum from shock-heated plasma; often with a harder bremsstrahlung component from a forward shock. This spectrum is easily distinguished from a power law shape. Only $\sim 7\%$ of ULX candidates *require* a thermal model to reproduce their spectra. As shown in § 3.2.1, about 15% of the ULX candidates with acceptable power law fits have steep slopes, $\Gamma \gtrsim 3$, suggesting a thermal spectrum. Thus, at least 22% of the ULX candidates are likely thermal sources. The actual number could be higher since a thermal model does provide a formally-acceptable fit to 78% of the ULX candidates. Nevertheless, it is unlikely that the majority of ULX candidates are thermal sources since the average power law model slope of 1.8 (or the average thermal model temperature of 18.4 keV) is much more descriptive of non-thermal sources.

Supernovae should be steady sources on short timescales and decline slowly over periods of months to years. Again, while results of variability tests are consistent with the majority of ULX candidates being steady sources, individual observations are too short to discern long-term trends and some low-level variability may be hidden in the low-count light curves. Variability has been reported for several ULX candidates based on multi-epoch monitoring (e.g., Fabbiano et al. 2003; Roberts et al. 2004, La Parola et al. 2001). In combination with detailed spectral modeling and radio wavelength imaging, the number of energetic supernovae contributing to the ULX population should soon be much better constrained. Core collapse supernovae have massive star progenitors consistent with the association of ULXs with late-type star-forming galaxies.

4.2. ULXs and their Host Galaxies

It has long been known (David, Jones, & Forman 1992) and recently confirmed (Ranalli, Comastri, & Setti 2002; Grimm, Gilfanov, & Sunyaev 2003) that the total X-ray luminosity of a galaxy correlates with recent star formation rate as measured by its far-infrared luminosity, L_{FIR} . We have shown that this trend extends to the numbers and total luminosities of ULXs found in such galaxies. This result was anticipated by the large numbers of ULXs in some FIR-bright galaxies (e.g., NGC 4038/4039, Zezas et al. 2002; NGC 3256 Lira et al. 2002; NGC 4485/4490, Roberts et al. 2002) and for a small sample of galaxies by Grimm, Gilfanov, & Sunyaev (2003). A similar conclusion can be indirectly deduced through studies of the cumulative X-ray luminosity functions of nearby galaxies: The flat slopes of the XLFs implies that the most luminous sources dominate the total X-ray luminosity of spiral and starburst galaxies (e.g., Kilgard et al. 2002; Grimm et al. 2003; Colbert et al. 2004).

Two of the theoretical explanations for ULXs discussed in the previous section predict an association of ULXs with recent star formation. These are the mildly-beamed

thermal-timescale mass transfer X-ray binaries described by King et al. (2001) and X-ray bright supernovae. While a case might be envisioned for IMBHs formed in prompt collapse of the cores of young super-star clusters, studies of the Antennae by Zezas et al. (2002, see also Clark et al. 2003) and of three other starburst galaxies by Kaaret et al. (2003) determined ULXs are often near but not spatially coincident with these clusters as would be expected if they are IMBH binaries. Recent numerical simulations (Portegies Zwart et al. 2004) indicate the formation frequency of IMBHs in super-star clusters depends sensitively on cluster initial conditions and dynamical friction timescale and thus does not simply scale with the host galaxy's (global) star formation rate. As only a small fraction of ULX candidates in our survey display the requisite thermal emission-line spectrum characteristic of supernovae, there remains only the model of King et al. (2001) as a reasonable representation of the *majority* of ULXs.

Does the model of King et al. (2001) provide a viable explanation for the results of the present survey? The model is essentially that of a high-mass X-ray binary (HMXRB) undergoing an episode of thermal-timescale mass transfer. Such systems arise when the donor star envelope is in a radiative phase either when it is more massive than its companion or first fills its Roche lobe while expanding to the red giant stage. Particulars of the mass transfer mechanism, possibilities of common envelope formation, and details of beaming and resulting luminosities are beyond the scope of the present work. However, the question remains if enough systems of this type occur to account for the numbers of ULXs reported here.

Assuming $\sim 2\%$ of OB stars form HMXRBs (e.g. Dalton & Sarazin 1995, Helfand & Moran 2001), that the thermal-timescale phase always occurs and lasts $\sim 10^5$ yr (King et al. 2001) or 1% of the lifetime of a star ($10\text{--}40$ Myr for stars of initial mass $8\text{--}20 M_{\odot}$), and a beaming factor $b = 0.1$; then at least $\sim 5 \times 10^4$ OB stars per ULX are required. From results of evolutionary synthesis models, Leitherer & Heckman (1995) find this many O stars are formed for a star formation rate (SFR) of $\sim 2 M_{\odot}$ yr $^{-1}$ over a period of >10 Myr. This result is for a particular choice of initial mass function, metallicity, upper mass cutoff, and star formation time-scale representative of conditions found in infrared-luminous starburst galaxies. The relation between L_{FIR} and SFR deduced by Leitherer & Heckman (1995) is⁹ $\text{SFR} = 0.045 (L_{\text{FIR}}/10^{42}) M_{\odot}$ yr $^{-1}$ (see also Kennicutt 1998). These values predict ~ 2 to 5 ULXs per $L_{\text{FIR}} = 10^{44}$ ergs s $^{-1}$, though the uncertainties are large. From §3.3, the number of ULXs per (spiral) galaxy is ~ 1 for galaxies with $L_{\text{FIR}} \sim 10^{43}$ ergs s $^{-1}$ rising to ~ 5 for $L_{\text{FIR}} \gtrsim 10^{44}$ ergs s $^{-1}$. Thus, the number of ULXs in high L_{FIR} galaxies follows the trend expected for a short-lived high stellar mass origin. Leitherer & Heckman (1995) also predict a peak massive-star supernova rate of 0.02 yr $^{-1}$ at a SFR of $1 M_{\odot}$ yr $^{-1}$ which will also contribute to the ULX population of active star-forming galaxies in proportion to L_{FIR} .

For lower L_{FIR} , and particularly for elliptical galax-

⁹ L_{FIR} in this expression is the $8\text{--}1000 \mu\text{m}$ luminosity which is about 50–100% larger than the $42.5\text{--}122.5 \mu\text{m}$ luminosities listed in Table 2 assuming a warm dust temperature.

ies, the number of ULXs is larger than this simple estimate predicts. Being dominated by the elliptical galaxies, ULXs in this group are correlated most strongly with the host galaxy's L_B . The number of ULX candidates per elliptical galaxy scales roughly as $N_{\text{ULX}} \sim 0.1 (L_B/10^{42})$ (§ 3.3). It is thus natural to relate the lower-luminosity ULXs to the long-lived population of stars, namely, to the low-mass X-ray binaries (LMXRBs). ULX candidates in weak L_{FIR} galaxies are also less-luminous than those in active star-forming galaxies as the average ULX luminosity also correlates with L_{FIR} (§ 3.3). The XLFs depicted in Figure 14 show that the ULXs in ellipticals are less-luminous than those in spirals. Irwin, Athey, & Bregman (2003) and Irwin, Bregman, & Athey (2004) show further that all ULX candidates in elliptical galaxies more luminous than 2×10^{39} ergs s^{-1} are likely background sources.

LMXRBs with stellar-mass ($M \sim 10\text{--}15 M_\odot$) BH accretors can reach luminosities of $\sim 2 \times 10^{39}$ ergs s^{-1} without violating the Eddington limit. The difficulty is achieving accretion rates of up to $\sim 10^{-6} M_\odot \text{ yr}^{-1}$. Although such high rates are seen in the soft X-ray transients (King 2002; Terashima & Wilson 2004), persistent sources within our Galaxy do not achieve this rate. A typical Galactic LMXRB radiating at a few 10^{37} ergs s^{-1} has an accretion rate of $\sim 10^{-8} M_\odot \text{ yr}^{-1}$ and can maintain this luminosity for $M/\dot{M} \sim 10^8$ yr for a $1 M_\odot$ mass-donor star. If all accretion rates are equally likely, then the probability of observing a ULX in a single observation would be inversely proportional to the lifetime at that accretion rate (e.g., Wu 2001). For this assumption, a luminosity of $\sim 10^{37}$ ergs s^{-1} is expected to be 100 times more common than $\sim 10^{39}$ ergs s^{-1} . This is consistent with what is inferred from the ULX cumulative luminosity function for ellipticals, Figure 14: There is one ULX per 100 X-ray sources above 6.3×10^{37} ergs s^{-1} . Of order 100 X-ray sources per $L_B = 10^{43}$ ergs s^{-1} are routinely detected above a few 10^{37} ergs s^{-1} in elliptical galaxies (e.g., NGC 4697, Sarazin et al. 2001) and in the bulges of spiral galaxies (e.g., NGC 3031, Swartz et al. 2003). The average blue luminosity of the elliptical galaxies in our sample is $(18 \pm 3) \times 10^{42}$ (Figure 4). Thus, the observed rate of ~ 2 ULX candidates per elliptical galaxy (or 1 ULX candidate per $L_B = 10^{43}$ ergs s^{-1}) is consistent with a LMXRB origin. The actual number is somewhat less since nearly 50% of the ULX candidates in elliptical galaxies are potentially background sources (§ 3.2.5) but this line of reasoning suggests that the dominant factor determining the slope of the cumulative X-ray luminosity function for ellipticals is simply the lifetimes of the LMXRBs.

Low-mass XRBs also exist in spiral galaxies. However, inspection of Figure 4 shows that, for spirals, L_B is more a measure of the young stellar content than of the total number of stars (or galaxy mass). Thus, while the contribution of LMXRBs to the ULX population is expected to scale with galaxy mass, it may not vary linearly with L_B for spirals in the present sample. Colbert et al. (2004) used B and K_s luminosities as a measure of galaxy mass to conclude that more than 20% of ULXs in spiral galaxies originate from the older stellar population.

Arguments for contributions from the young and the old stellar populations to the total X-ray luminosity of

nearby galaxies have been made since the *Einstein* Observatory era (see the review by Fabbiano 1989). More recently, Colbert et al. (2004) show that X-ray point source populations can also be described as a superposition of contributions from these two stellar populations. Here it has been shown that the ULX candidate population also displays this dichotomy. Considering ULXs as a subset of all X-ray sources or, equivalently, as a subset of the total X-ray luminosity of a galaxy, this result supports the idea that ULXs are the high-luminosity end of a distribution of HMXRBs and supernovae and of LMXRBs.

4.3. Summary

X-ray properties and celestial positions of a sample of 154 ULX candidates have been tabulated. The X-ray properties alone are unable to discriminate between ULXs and the less-luminous population (to a formal completeness limit of $\sim 4 \times 10^{38}$ ergs s^{-1}). This could perhaps be foreseen since, for example, the power law indices of accreting X-ray sources ranging from stellar-mass neutron stars and black holes to supermassive active galactic nuclei are, on average, comparable to the mean power law index, $\Gamma = 1.74 \pm 0.03$, obtained here for ULX candidates. Based on spectral shape, namely a steep power law index or, equivalently, a cool plasma temperature, about 20% of the ULX candidates are potentially supernovae but this group also includes a few variable and/or supersoft sources. The supersoft (or 'quasisoft') spectra may be a signature of IMBHs as these objects are expected to have a soft blackbody disk component. Most of the sources studied here, however, can be described by a simple power law and do not require an additional (soft) thermal component. Future spectrophotometric X-ray observations will help distinguish between transient XRBs and slowly-evolving young supernovae but optical and radio data (and rapidly-sampled X-ray timing data) will be needed to discern, e.g., beamed sources from IMBHs. The precise source locations provided by *Chandra* should be a tremendous aid to such followup observations.

The number of ULX candidates per galaxy is roughly the same for spirals and ellipticals but the luminosities of the ULXs are ~ 10 times higher in spirals compared to ellipticals and the ULX candidate population in ellipticals is severely compromised by background sources (estimated to be 44% in the present sample compared to only 14% for spirals). There is also a strong correlation between the number and average luminosity of ULXs in spirals and their host galaxy's far-infrared luminosity; and a weaker (anti-)correlation with nearest-neighbor distance.

The X-ray data do not favor any particular model for ULX phenomena. The similarity to properties of weaker sources strongly suggests ULXs are not a distinct class but composed of a heterogeneous mixture as are the weaker sources; in which case all models remain viable on a case by case basis. The association with recent star formation, and the significant lack of bright ULXs in elliptical galaxies, does make a strong case for young, short-lived, systems such as HMXRBs as the dominant component of the more luminous ULX population. On the other hand, the population of ULXs in ellipticals and at least some of the ULXs in spirals can be explained as the high-luminosity end of the LMXRB population.

The intrinsic luminosities of the ULX candidates in the

sample range up to $\sim 10 \times 10^{39}$ ergs s $^{-1}$ in the 0.5–8.0 keV band, the point where the luminosity function rolls over, with a few objects radiating at even higher luminosities. The Eddington luminosity limit thus requires accretor masses of order 80 M_{\odot} and possibly even higher. Stellar-mass BHs can form with masses up to $\sim 20 M_{\odot}$ (Fryer & Kalogera 2001). If a companion of high initial mass can add some 10–20 M_{\odot} during a phase of super-Eddington accretion and the system is observed near the endpoint of this phase, then the luminosity of such a high mass X-ray binary could readily be of order 10×10^{39} ergs s $^{-1}$ if the Eddington limit is exceeded by modest amounts and a high accretion rate can be achieved. While it may still be difficult to attain the highest luminosities inferred in the current study, this need only occur rarely to account for the handful of very luminous ULXs (among the thousands of sources detected).

We thank Roberto Soria for discussions on the nature of ULXs and Jimmy Irwin for insightful conversations on the role of background sources in the fields

of elliptical galaxies. We thank the referee for a thorough critique of the manuscript and an alternative perspective on many key points. This research has made use of the NASA/IPAC Extragalactic Database (NED) which is operated by the Jet Propulsion Laboratory, California Institute of Technology, under contract with NASA; of Second Palomar Observatory Sky Survey (POSS-II) images made by the California Institute of Technology with funds from the NSF, NASA, the National Geographic Society, the Sloan Foundation, the Samuel Oschin Foundation, and the Eastman Kodak Corporation; of Digitized Sky Survey images produced at the Space Telescope Science Institute under U.S. Government grant NAG W-2166; of the *Chandra* X-ray Center ObsID-based literature search engine, <http://asc.harvard.edu/cda/bib.html>; and of software obtained from the High Energy Astrophysics Science Archive Research Center (HEASARC), provided by NASA's Goddard Space Flight Center. Support for this research was provided in part by NASA/*Chandra* grant AR2-3008X.

REFERENCES

- Abramowicz, M. A., Czerny, B., Lasota, J. P., & Szuszkiewicz, E. 1988, *ApJ*, 332, 646
- Aldcroft, T. L., Karovska, M., Cresitello-Dittmar, M. L., Cameron, R. A., & Markevitch, M. L. 2000, *SPiE*, 4012, 650
- Blanton, E. L., Sarazin, C. L., & Irwin, J. A. 2001, *ApJ*, 552, 106
- Brandt, W. N., et al. 2001, *AJ*, 122, 2810
- Bregman, J. N., & Irwin, J. A. 2002, *ApJ*, 565, L13
- Cagnoni, I., Turolla, R., Treves, A., Huang, J.-S., Kim, D. W., Elvis, M., & Celotti, A. 2003, *ApJ*, 582, 654
- Cecil, G., Bland-Hawthorn, J., & Veilleux, S. 2002, *ApJ*, 576, 745
- Clark, D. M., et al. 2003, *BAAS*, 203, 122.03
- Colbert, E. J. M., Heckman, T. M., Ptak, A. F., Strickland, D. K., & Weaver, K. A. 2004, *ApJ*, in press.
- Colbert, E. J. M., & Mushotzky, R. F. 1999, *ApJ*, 519, 89
- Colbert, E. J. M., & Ptak, A. F. 2002, *ApJS*, 143, 25
- Collinge, M. J., et al. 2001, *ApJ*, 557, 2
- Dalton, W. W., & Sarazin, C. L. 1995, *ApJ*, 440, 280
- David, L. P., Jones, C., & Forman, W. 1992, *ApJ*, 388, 82
- Davis, J. E. 2001, *ApJ*, 562, 575
- Davis, J. E. 2002, <http://space.mit.edu/CXC/analysis/davis/head2002/>
- de Vaucouleurs, G. 1978, *ApJ*, 223, 351
- de Vaucouleurs G., de Vaucouleurs A., Corwin Jr. H. G., Buta R. J., Paturel G., & Fouque P. 1991, *Third Reference Catalogue of Bright Galaxies* (New York: Springer-Verlag)
- Dickey, J. M. & Lockman, F. J. 1990, *ARAA*, 28, 215
- Di Stefano, R. D., Kong, A. K. H., VanDalsen, M. L., Harris, W. E., Murray, S. S., & Delain, K. M. 2003, *ApJ*, 599, 1067
- Ebisawa, K., Zycki, P., Kubota, A., Mizuno, T., & Watarai, K. -Y. 2003, *ApJ*, 597, 780
- Ebisuzaki, T. et al. 2001 *ApJ*, 562, L19
- Eracleous, M., Shields, J. C., Chartas, G., & Moran, E. C. 2002, *ApJ*, 565, 108
- Fabbiano, G. 1989, *ARA&A*, 27, 87
- Fabbiano, G., & Trinchieri, G. 1985, *ApJ*, 296, 430
- Fabbiano, G., & Shapley, A. 2002, *ApJ*, 565, 908
- Fabbiano, G., Zezas, A., & Murray, S. S. 2001, *ApJ*, 554, 1035
- Fabbiano, G., Zezas, A., King, A. R., Ponman, T. J., Rots, A., & Schweizer, F. 2003, *ApJ*, 584, L5
- Fabbiano, G. et al. 2003, *ApJ*, 588, 175
- Fabrika, S., & Mescheryakov, A. 2001, *IAUS*, 205, 268
- Fasano, G., & Franceschini, A. 1987, *MNRAS*, 225, 155
- Ferrarese, L., et al. 2000, *ApJ*, 529, 745
- Finoguenov, A., & Jones, C. 2002 *ApJ*, 574, 754
- Foschini, L., et al. 2002, *A&A*, 392, 817
- Fryer, C. L., & Kalogera, V. 2001, *ApJ* 554, 548
- Georganopoulos, M., Aharonian, F. A., & Kirk, J. G., 2002 *A&A*, 388, L25
- Grimm, H. -J., Gilfanov, M., & Sunyaev, R. 2003, *MNRAS*, 339, 793
- Heike, K., Awaki, H., Misao, Y., Hayashida, K., & Weaver, K. A. 2003, *ApJ*, 591, L99
- Helfand, D. J. 1984, *PASP*, 96, 913
- Helfand, D. J., & Moran, E. C. 2001, *ApJ*, 554, 27
- Ho, L. C., Filippenko, A. V., & Sargent, W. L. W. 1997, *ApJS*, 112, 315
- Holt, S. S., Schlegel, E. M., Hwang, U., & Petre, R. 2003, *ApJ*, 588, 792
- Humphrey, P. J., Fabbiano, G., Elvis, M., Church, M. J., & Balucinska-Church, M. 2003, *MNRAS*, 344, 134
- Immler, S., & Lewin, W. H. G. 2003, in *Supernovae and Gamma-Ray Bursters*, ed. K. Weiler (Heidelberg:Springer-Verlag), 91
- Irwin, J. A., Athey, A. E., & Bregman, J. N. 2003, *ApJ*, 587, 256
- Irwin, J. A., Bregman, J. N., & Athey, A. E. 2004, *ApJ*, 601, L143
- Irwin, J. A., Sarazin, C. L., & Bregman, J. N. 2002, *ApJ*, 570, 152
- Iwasawa, K., Wilson, A. S., Fabian, A. C., & Young, A. J. 2003, *MNRAS*, 345, 369
- Jeltema, T. E., Canizares, C. R., Buote, D. A., & Garmire, G. P. 2003, *ApJ*, 585, 756
- Jimnez-Bailn, E. et al. 2003, *ApJ*, 593, 127
- Jones, C. et al. 2002, *ApJ*, 567, L115
- Kaaret, P., Alonso-Herrero, A., Gallagher, J. S., III, Fabbiano, G., Zezas, A., & Rieke, M. J. 2004, *MNRAS*, 348, L28
- Kalogera, V., Henninger, M., Ivanova, N., & King, A. R. 2004, *ApJ*, 603, L41
- Karachentsev, I. D., & Tikhonov, N. A. 1994, *A&A* 286, 718
- Kennicutt, R. C., Jr. 1998, *ARA&A*, 36, 189
- Kilgard, R. E., Kaaret, P., Krauss, M. I., Prestwich, A. H., Raley, M. T., & Zezas, A. 2002, *ApJ*, 573, 138
- Kim, D. W., & Fabbiano, G. 2003, *ApJ*, 586, 826
- King, A. R., 2002, *MNRAS*, 335, L13

- King, A. R., Davies, M. B., Ward, M. J., Fabbiano, G., & Elvis, M. 2001, *ApJ*, 552, L109
- Knapp, G. R., Guhathakurta, P., Kim, D. -W., & Jura, M. 1989, *ApJS*, 70, 329
- Körding, E., Falcke, H., & Markoff, S. 2002, *A&A*, 382, L13
- Kong, A. K. H., Garcia, M. R., Primini, F. A., Murray, S. S., Di Stefano, R., & McClintock, J. E. 2002, *ApJ*, 577, 738
- Kraft, R. P., Kregenow, J. M., Forman, W. R., Jones, C., & Murray, S. S. 2001, *ApJ*, 560, 675
- Kubota, A., et al. 2001, *ApJ*, 547, L119
- Kundu, A., Maccarone, T. J., Zepf, S. E., & Puzia, T. H. 2003, *ApJ*, 589, L81
- La Parola, V., Peres, G., Fabbiano, G., Kim, D. -W., & Bocchino, F. 2001, *ApJ*, 556, 47
- Leahy, D. A., Darbro, W., Elsner, R. F., Weisskopf, M. C., Kahn, S., Sutherland, P. G., & Grindlay, J. E. 1983, *ApJ*, 266, 160
- Leitherer, C. & Heckman, T. M. 1995, *ApJS*, 96, 9
- Lira, P., Ward, M., Zezas, A., Alonso-Herrero, A., & Ueno, S. 2002, *MNRAS*, 330, 259
- Liu, J. F., Bregman, J. N., Irwin, J., & Seitzer, P. 2002, *ApJ*, 581, L93
- Long, K. S., & van Speybroeck, L. P. 1983, in *Accretion-Driven X-Ray Sources*, ed. W. H. G. Lewin, & E. P. J. van den Heuvel (Cambridge: Cambridge Univ. Press) 117
- Maccarone, T. J., Kundu, A., & Zepf, S. E. 2003, *ApJ*, 586, 814
- Madau, P., 1988, *ApJ*, 327, 116
- Madau, P., & Rees, M. J. 2001, *ApJ*, 551, L27
- Makishima, K., et al. 2000, *ApJ*, 535, 632
- Matsumoto, H. et al. 2001, *ApJ*, 547, L25
- McClintock, J. E., & Remillard, R. A. 2003, *astro-ph/0306213*
- McDowell, J. C., Fabbiano, G., Kalogera, V., Stanek, K., & Sasselov, D. 2000, *Proceedings 232, WE-Heraeus Seminar*, Eds. E. M. Berkhuysen, R. Beck, and R. A. M. Walterbos, (Shaker:Aachen)
- Miller, J. M., Fabbiano, G., Miller, M. C., & Fabian, A. C. 2003, *ApJ*, 585, L40
- Miller, M. C., & Hamilton, D. P. 2002, 330, 232
- Miller, M. C., & Colbert, E. J. M. 2003, *astro-ph/0308402*
- Mukai, K. 1993, *Legacy*, 3, 21
- Mukai, K., Pence, W. D., Snowden, S. L., & Kuntz, K. D. 2003, *ApJ*, 582, 184
- Ogasaka, Y. et al. 1998, *AN*, 319, 43
- Ott, J., Martin, C. L., & Walter, F. 2003, *ApJ*, 594, 776
- Ptak, A., & Colbert, E. 2004, *ApJ*, 606, 291
- Peacock, J. A. 1983, *MNRAS*, 202, 615
- Pellegrini, S., Fabbiano, G., Fiore, F., Trinchieri, G., & Antonelli, A. 2002, *A&A*, 383, 1
- Portegies Zwart, S. F., & McMillian, S. L. W. 2002, *ApJ*, 576, 899
- Portegies Zwart, S. F., Baumgardt, H., Hut, P., Makino, J., & McMillian, S. L. W. 2004, *Nature*, 428, 724
- Prestwich, A. H., et al. 2003, *ApJ*, 595, 719
- Ranalli, P., Comastri, A., & Setti, G. 2002, *A&A*, 399, 39
- Rice, W., et al. 1988, *ApJS*, 68, 91
- Roberts, T. P., & Colbert, E. J. M. 2003, *MNRAS*, 341, L49
- Roberts, T. P., Goad, M. R., Ward, M. J., Warwick, R. S., O'Brien, P. T., Lira, P., & Hands, A. D. P. 2001, *MNRAS*, 325, L7
- Roberts, T. P., & Warwick, R. S. 2000, *MNRAS*, 315, 98
- Roberts, T. P., Warwick, R. S., Ward, M. J., & Goad, M. R. 2004, *MNRAS*, 349, 1193
- Roberts, T. P., Warwick, R. S., Ward, M. J., & Murray, S. S. 2002, *MNRAS*, 337, 677
- Rosati, P., et al. 2002, *ApJ*, 566, 667
- Sarazin, C. L., Irwin, J. A., & Bregman, J. N. 2001 *ApJ*, 556, 533
- Schlegel, E. M. 1995, *Rep. Prog. Phys.*, 58, 1375
- Schlegel, E. M. 2001, *ApJ*, 556, L25
- Schlegel, E. M., & Pannuti, T. G. 2003, *AJ*, 125, 3025
- Schurch, N. J., Roberts, T. P., & Warwick, R. S. 2002, *MNRAS*, 335, 241
- Sivakoff, G. R., Sarazin, C. L., & Irwin, J. A. 2003, *ApJ*, 599, 218
- Smith, D. A., & Wilson, A. S. 2001, *ApJ*, 557, 180
- Smith, D. A., & Wilson, A. S. 2003, *ApJ*, 591, 138
- Soria, R., & Wu, K. 2002, *A&A*, 384, 99
- Strickland, D. K., Colbert, E. J. M., Heckman, T. M., Weaver, K. A., Dahlem, M., & Stevens, I. R. 2001, *ApJ*, 560, 707
- Strickland, D. K., Heckman, T. M., Weaver, K. A., & Dahlem, M. 2000, *AJ*, 120, 2965
- Summers, L. K., Stevens, I. R., Strickland, D. K., & Heckman, T. M. 2003 *MNRAS*, 342, 690
- Swartz, D. A., Ghosh, K. K., McCollough, M. L., Pannuti, T. G., Tennant, A. F., & Wu, K. 2003, *ApJS*, 144, 213
- Terashima, Y., & Wilson, A. S. 2004, *ApJ*, 601, 735
- Terlevich, R., Melnick, J., & Moles, M. 1987, *IAUS*, 121, 499
- Terlevich, R., Tenorio-Tagle, G., Franco, J., & Melnick, J. 1992, *MNRAS*, 255, 713
- Townsley, L. K., Broos, P. S., Garmire, G. P., & Nousek, J. A. 2000, *ApJ*, 534, L139
- Trinchieri, G., Sulentic, J., Breitschwerdt, D., & Pietsch, W. 2003, *A&A*, 401, 173
- Tully, R. B. 1988, *Nearby Galaxies Catalogue* (Cambridge:Cambridge University Press)
- Tully, R. B., & Shaya, E. J. 1984, *ApJ*, 281, 31
- Ueda, Y., et al. 1998, *AN*, 319, 47
- van der Marel, R. P. 2004, in *Coevolution of Black Holes and Galaxies*, ed. L. C. Ho, (Cambridge:Cambridge), 37
- Wang, Q. D. 1999, *ApJ*, 517, L27
- Wang, Q. D., Chaves, T., & Irwin, J. 2003, *ApJ*, 598, 969
- Wang, Q. D., Immler, S., Walterbos, R., Lauroesch, J. T., & Breitschwerdt, D. 2001, *ApJ*, 555, L99
- Watarai, K. -Y., Mizuno, T., & Mineshige, S. 2001, *ApJ*, 549, L77
- Wilson, A. S., & Yang, Y. 2002, *ApJ*, 568, 133
- Wilson, A. S., Yang, Y., & Cecil, G. 2001, *ApJ*, 560, 689
- Wu, K. 2001, *PASA*, 18, 443
- Yang, Y., Wilson, A. S., & Ferruit, P. 2001, *ApJ*, 563, 124
- Zezas, A., Fabbiano, G., Rots, A. H., & Murray, S. S. 2002, *ApJ*, 577, 710
- Zombeck, M. V. 1990, *Handbook of Astronomy and Astrophysics*, Second Edition (Cambridge, UK: Cambridge University Press)

TABLE 1
PROPERTIES OF SAMPLE GALAXIES & X-RAY OBSERVATION SUMMARY

Galaxy	Type	Distance ^a (Mpc)	$L_B/10^{42}$ (erg s ⁻¹)	$L_{FIR}/10^{42}$ (erg s ⁻¹)	θ_p^b	ObsID	Date	t_{exp} (ks)	f_{FOV}	$L_{min}/10^{37}$ (erg s ⁻¹)	Ref.
NGC 0253	SAB(s)c	2.6 t	7.64	4.55	5.2	969	1999-12-16	14.0	0.59	2.8	1
NGC 0278	SAB(rs)b	11.8 v	5.82	21.97	138.8	2055	2001-06-22	38.3	1.00	28.6	
NGC 0404	SA(s)0-	3.0 T	0.30	0.14	83.6	870	1999-12-19	23.9	1.00	2.5	2
NGC 0598	SA(s)cd	0.9 C	2.81	2.55	4.1	786	2000-08-30	46.3	0.18	0.1	3
NGC 0628	SA(s)c	9.7 v	9.10	17.04	27.7	2058	2001-10-19	46.2	0.93	13.1	
NGC 0720	E5	24.6 I	16.57	0.07	5.9	492	2000-10-12	39.6	1.00	88.6	4
NGC 0891	SA(s)b	10.0 P	13.85	53.46	15.4	794	2000-11-01	50.9	0.82	13.6	5
NGC 1068	(R)SA(rs)b	14.4 v	26.19	221.17	4.3	344	2000-02-21	47.4	1.00	27.0	6
NGC 1291	(R)SB(s)0/a	8.9 t	11.49	1.77	8.9	795	2000-06-27	39.2	0.79	12.0	7
NGC 1316	SAB(s)0(pec)	17.0 P	38.93	6.74	0.5	2022	2001-04-17	29.9	0.79	56.9	8
NGC 1399	E1(pec)	18.3 F	17.31	0.14	1.4	319	2000-01-18	55.9	1.00	34.5	9
NGC 1407	E0	17.6 G	12.49	0.37	1.8	791	2000-08-16	48.6	1.00	43.0	9
NGC 1549	E0-1	19.7 I	16.05	0.11	61.2	2077	2000-11-08	36.5	1.00	61.6	9
NGC 1553	SA(r)0	18.5 I	20.97	1.27	2.6	783	2000-01-02	33.7	1.00	59.0	10
NGC 1569	IBm	2.2 T	0.64	1.21	79.9	782	2000-04-11	96.8	1.00	0.5	11
NGC 2403	SAB(s)cd	3.1 C	3.22	4.16	13.3	2014	2001-04-17	35.6	0.53	1.8	12
UGC 4305	Im	3.4 T	0.41	0.10	13.5	1564	2001-11-02	5.1	0.31(1/4)	13.9	
NGC 2681	(R')SAB(rs)0/a	17.2 I	10.20	13.46	74.1	2060	2001-01-30	80.9	1.00	21.9	13
NGC 3031	SA(s)ab	3.6 C	11.30	5.73	1.4	735	2000-05-07	49.9	0.57	1.7	14
NGC 3034	I0	3.9 T	2.87	91.33	3.3	361	1999-09-20	33.3	1.00	2.5	15
NGC 3079	SB(s)c	15.6 v	12.93	85.95	22.8	2038	2001-03-07	26.6	1.00	51.8	16
NGC 3077	I0(pec)	4.0 I	0.81	1.59	8.7	2076	2001-03-07	53.4	1.00	1.9	17
NGC 3115	S0-	10.0 F	9.85	0.10	40.1	2040	2001-06-14	37.0	1.00	17.2	9
NGC 3184	SAB(rs)cd	14.4 C	11.83	16.51	31.7	804	2000-01-08	42.1	1.00	28.4	13,18
IC 2574	SAB(s)m	4.0 T	0.92	0.41	10.5	792	2000-01-07	10.0	0.58	9.5	13
NGC 3379	E1	11.1 F	8.12	0.12	1.4	1587	2001-02-13	31.5	1.00	23.7	
NGC 3507	SB(s)b	19.8 v	6.83	0.05	40.4	3149	2002-03-08	39.3	1.00	58.1	
NGC 3556	SB(s)cd	14.1 v	18.02	48.58	19.7	2025	2001-09-08	59.4	1.00	18.9	19
NGC 3585	E6	20.0 I	17.20	0.25	8.6	2078	2001-06-03	35.3	1.00	74.4	9
NGC 3607	SA(s)0	22.8 I	19.47	0.06	1.2	2073	2001-06-12	38.5	1.00	78.3	
NGC 3628	Sb(pec)	10.0 t	14.64	36.98	2.4	2039	2000-12-02	58.0	0.68	10.2	20
UGC 6456	Pec	4.4 T	0.03	0.00	—	871	2000-01-07	10.2	1.00(1/4)	11.8	
NGC 4038	SB(s)m(pec)	19.3 v	16.31	102.80	0.2	315	1999-12-01	72.2	1.00	16.5	21
						3040	2001-12-29	69.0	1.00		21
NGC 4039	SA(s)m(pec)	19.3 v	14.88	102.80	0.2	315	1999-12-01	72.2	1.00	16.5	21
						3040	2001-12-29	69.0	1.00		21
NGC 4051	SAB(rs)bc	9.7 v	3.69	7.27	11.6	2148	2001-02-06	45.8	0.32(1/8)	11.8	22
NGC 4111	SA(r)0+	15.0 I	2.27	0.02	9.3	1578	2001-04-03	14.8	1.00(1/2)	49.9	
NGC 4125	E6(pec)	24.2 I	24.49	2.92	32.4	2071	2001-09-09	64.2	1.00	53.5	
NGC 4151	(R')SAB(rs)ab	13.0 t	6.81	5.83	4.6	348	2000-03-07	27.6	1.00	36.1	23
NGC 4214	IAB(s)m	3.5 v	0.83	1.40	10.8	2030	2001-10-16	26.4	1.00	2.7	
NGC 4244	SA(s)cd	4.5 t	3.05	0.82	5.5	942	2000-05-20	49.1	1.00	2.4	24
NGC 4258	SAB(s)bc	7.7 I	17.94	12.14	11.6	1618	2001-05-28	20.9	0.61	16.4	25
NGC 4303	SAB(rs)bc	16.1 t	17.99	71.06	27.1	2149	2001-08-07	28.0	1.00	53.9	26

TABLE 1
Continued

Galaxy	Type	Distance ^a (Mpc)	$L_B/10^{42}$ (erg s ⁻¹)	$L_{FIR}/10^{42}$ (erg s ⁻¹)	θ_p^b	ObsID	Date	t_{exp} (ks)	f_{FOV}	$L_{min}/10^{37}$ (erg s ⁻¹)	Ref.
NGC 4314	SB(rs)a	13.1 t	4.53	4.39	9.3	2062	2001-04-02	16.1	1.00	31.3	
						2063	2001-06-22	16.1	1.00		
NGC 4365	E3	20.9 F	21.56	0.61	12.8	2015	2001-06-02	40.4	1.00	62.5	27
NGC 4374	E1	17.4 F	23.25	1.07	13.2	803	2000-05-19	28.5	1.00	63.8	28
NGC 4382	SA(s)0+(pec)	16.6 F	21.56	0.24	1.1	2016	2001-05-29	39.7	1.00	41.5	29
NGC 4388	SA(s)b	16.7 v	10.44	20.11	6.7	1619	2001-06-08	20.0	1.00	83.8	30
NGC 4395	SA(s)m	4.2 v	0.81	0.64	10.6	882	2000-06-20	16.7	0.31(1/2)	6.0	
NGC 4449	IBm	3.7 t	1.12	3.19	23.7	2031	2001-02-04	26.6	1.00	2.0	31
NGC 4472	E2	15.9 I	36.32	0.37	6.4	321	2000-06-12	39.6	0.95	37.2	32
NGC 4485	IB(s)m(pec)	7.8 v	0.61	0.78	1.6	1579	2000-11-03	19.5	1.00	18.2	33
NGC 4490	SB(s)d(pec)	7.8 v	5.62	19.15	0.6	1579	2000-11-03	19.5	1.00	18.2	33
NGC 4486	E0-1(pec)	15.8 F	30.95	0.52	10.8	352	2000-07-29	37.7	1.00	39.7	34
NGC 4494	E1-2	14.5 F	9.82	0.31	14.2	2079	2001-08-05	24.8	1.00	49.0	9
NGC 4552	E0-1	15.9 F	11.52	0.34	13.8	2072	2001-04-22	54.4	1.00	27.7	
NGC 4559	SAB(rs)cd	10.3 v	10.26	8.39	11.0	2027	2001-06-04	10.7	0.27(1/4)	57.4	
NGC 4579	SAB(rs)b	21.0 v	26.17	24.12	14.7	807	2000-05-02	33.9	0.47(1/4)	77.4	2
NGC 4594	SA(s)a	9.6 I	31.43	4.66	25.5	1586	2001-05-31	18.5	1.00	30.6	35
NGC 4621	E5	15.8 F	11.88	0.24	20.2	2068	2001-08-01	24.8	1.00	59.6	
NGC 4631	SB(s)d	7.6 v	16.11	37.12	13.8	797	2000-04-16	59.2	1.00	5.6	36
NGC 4636	E0-1	15.1 I	11.89	0.28	6.7	323	2000-01-26	52.4	1.00	25.5	37
NGC 4649	E2	16.6 F	28.16	1.25	12.0	785	2000-04-20	36.9	1.00	44.2	9
NGC 4697	E6	11.8 I	10.03	0.48	2.1	784	2000-01-15	39.3	1.00	20.8	38
NGC 4736	(R)SA(r)ab	5.2 I	6.63	12.02	20.5	808	2000-05-13	47.4	0.19(1/4)	3.3	39
NGC 4945	SB(s)cd	3.7 t	11.32	60.87	1.2	864	2000-01-27	49.1	1.00	2.4	40
NGC 5055	SA(rs)bc	9.2 t	16.03	33.54	22.6	2197	2001-08-27	28.0	0.89	17.4	
NGC 5102	SA0-	3.5 v	0.96	0.09	100.0	2949	2002-05-21	34.2	1.00	2.3	
NGC 5128	S0(pec)	4.0 F	14.91	25.83	3.7	962	2000-05-17	36.5	0.67	3.1	41
NGC 5204	SA(s)m	4.5 t	0.40	0.35	47.0	2029	2001-05-02	9.0	0.27(1/8)	12.9	42
NGC 5194	SA(s)bc(pec)	8.4 P	24.32	79.90	0.4	1622	2001-06-23	26.8	0.95	19.9	43
NGC 5236	SAB(s)c	3.7 T	6.82	27.19	2.2	793	2000-04-29	51.0	0.79	1.7	44
NGC 5253	Pec	3.2 C	0.51	1.65	10.7	2032	2001-01-13	56.6	1.00	1.2	
NGC 5457	SAB(rs)cd	7.0 C	19.98	35.74	10.1	934	2000-03-26	98.2	0.53	2.9	45
Circinus	SA(s)b	4.0 v	4.94	23.02	3.1	356	2000-03-14	23.1	1.00	9.8	46
NGC 5774	SAB(rs)d	26.8 v	4.86	4.54	1.0	2940	2002-04-05	58.2	1.00	76.2	
NGC 5775	SBc	26.7 v	17.96	120.51	1.0	2940	2002-04-05	58.2	1.00	75.6	
NGC 6503	SA(s)cd	4.1 t	1.18	1.39	41.0	872	2000-03-23	13.2	1.00	8.0	
NGC 6946	SAB(rs)cd	5.5 t	18.12	31.53	25.3	1043	2001-09-07	58.3	0.87	4.8	47
NGC 7320	SA(s)d	13.8 v	1.41	1.37	13.9	789	2000-07-09	19.7	1.00	68.3	48
NGC 7331	SA(s)b	14.6 C	29.33	65.75	27.7	2198	2001-01-27	29.5	0.62(1/2)	51.4	
IC 1459	E3-4	29.2 I	18.43	1.85	1.2	2196	2001-08-12	58.8	1.00(1/2)	49.8	49
IC 5332	SA(s)d	9.4 v	2.94	0.96	14.4	2066	2001-05-02	52.1	1.00	9.8	13

REFERENCES. — (1) Strickland et al. 2000; (2) Eracleous et al. 2002; (3) McDowell et al. 2000; (4) Jeltama et al. 2003; (5) Bregman & Irwin 2002; (6) Smith & Wilson 2003; (7) Irwin, Sarazin & Bregman 2002; (8) Kim & Fabbiano 2003; (9) Irwin, Athey & Bregman 2003; (10) Blanton, Sarazin & Irwin 2001; (11) Heike et al. 2003; (12) Schlegel & Pannuti 2003; (13) Humphrey et al. 2003; (14) Swartz et al. 2003; (15) Matsumoto et al. 2001; (16) Cecil, Bland-Hawthorn & Veilleux 2002; (17) Ott, Martin & Walter 2003; (18) Schlegel 2001; (19) Wang, Chaves & Irwin 2003; (20) Strickland et al. 2001; (21) Fabbiano, Zezas & Murray 2001; (22) Collinge et al. 2001; (23) Yang, Wilson & Ferruit 2001; (24) Cagnoni et al. 2003; (25) Wilson, Yang & Cecil 2001; (26) Jimenez-Bailn et al. 2003; (27) Kundu et al. 2003; (28) Finoguenov & Jones 2002; (29) Sivakoff, Sarazin & Irwin 2003; (30) Iwasawa et al. 2003; (31) Summers et al. 2003; (32) Maccarone, Kundu & Zepf 2003; (33) Roberts et al. 2002; (34) Wilson & Yang 2002; (35) Di Stefano et al. 2003; (36) Wang et al. 2001; (37) Jones et al. 2002; (38) Sarazin, Irwin & Bregman 2001; (39) Pellegrini et al. 2002; (40) Schurch, Roberts & Warwick 2002; (41) Kraft et al. 2001; (42) Roberts et al. 2001; (43) Liu et al. 2002; (44) Soria & Wu 2002; (45) Mukai et al. 2003; (46) Smith & Wilson 2001; (47) Holt et al. 2003; (48) Trinchieri et al. 2003; (49) Fabbiano et al. 2003

^aC:Cepheid period-luminosity; I:I-band SBF; T:Tip of RGB; P:Pla netary nebula luminosity function; G:Globular cluster luminosity function; t:ter tiary estimators; v:Tully-Fisher and variants including Tully (1988); F:average of primary estimators from Ferrerese et al. (2000)

^bNearest-neighbor distance in units of the D_{25} diameter

TABLE 2
PROPERTIES OF ULX CANDIDATES

Galaxy	R.A. (h m s)	Decl. (d m s)	Spectral ^a Parameter	n_H (10^{22} cm $^{-2}$)	χ^2/dof	L_{obs} (10^{39} erg s $^{-1}$)	L_{int} (10^{39} erg s $^{-1}$)	($H - M$) color	($M - S$) color	P_{KS}
NGC 628	1 36 51.06	+15 45 46.8	$2.01^{+0.12}_{-0.12}$	$0.05^{+0.00}_{-0.00}$	41.06/35	1.50 ± 0.08	1.78 ± 0.08	-0.17	-0.12	0.001
NGC 720	1 52 55.86	-13 43 51.1	$1.56^{+0.50}_{-0.42}$	$0.01^{+0.00}_{-0.00}$	3.19/5	0.99 ± 0.22	1.08 ± 0.24	-0.05	-0.14	0.521
NGC 720	1 52 56.54	-13 43 47.8	$1.78^{+1.24}_{-0.82}$	$0.27^{+0.75}_{-0.27}$	4.38/3	1.16 ± 0.24	1.57 ± 0.52	-0.13	0.28	0.712
NGC 720	1 52 59.44	-13 43 57.5	$2.33^{+0.98}_{-0.71}$	$0.14^{+0.23}_{-0.14}$	2.04/2	1.07 ± 0.19	1.46 ± 0.34	-0.25	-0.09	0.637
NGC 720	1 53 06.48	-13 45 40.9	$1.79^{+0.92}_{-0.60}$	$0.13^{+0.28}_{-0.13}$	3.55/4	1.12 ± 0.23	1.32 ± 0.22	-0.17	0.16	0.274
NGC 891	2 22 31.25	+42 19 57.8	$3.55^{+0.41}_{-0.55}$ c	$0.61^{+0.05}_{-0.03}$	62.21/60	4.05 ± 0.26	5.96 ± 0.25	-0.22	0.40	0.688
NGC 891	2 22 31.35	+42 20 24.4	$1.93^{+0.14}_{-0.13}$	$0.69^{+0.08}_{-0.07}$	79.88/77	5.03 ± 0.16	8.33 ± 0.35	-0.08	0.42	0.603
NGC 1068	2 42 38.89	-00 00 55.1	$0.97^{+0.15}_{-0.14}$	$0.63^{+0.13}_{-0.10}$	75.10/61	11.33 ± 0.42	13.51 ± 0.47	0.28	0.31	0.822
NGC 1068	2 42 39.71	-00 01 01.4	$1.04^{+0.12}_{-0.13}$ b	$0.04^{+0.04}_{-0.04}$	20.82/20	1.43 ± 0.09	1.49 ± 0.11	-0.25	0.09	0.198
NGC 1068	2 42 40.47	-00 00 51.9	$4.03^{+0.95}_{-0.71}$	$0.45^{+0.18}_{-0.14}$	12.20/16	0.63 ± 0.08	3.07 ± 1.35	-0.39	0.02	0.613
NGC 1291	3 17 02.53	-41 07 14.0	$2.93^{+0.37}_{-0.32}$	$0.24^{+0.08}_{-0.07}$	20.78/20	0.62 ± 0.04	1.21 ± 0.16	-0.30	-0.09	0.715
NGC 1291	3 17 13.82	-41 10 34.6	$2.32^{+0.31}_{-0.27}$	$0.15^{+0.07}_{-0.07}$	19.20/20	0.84 ± 0.06	1.17 ± 0.10	-0.28	-0.01	0.700
NGC 1316	3 22 41.07	-37 12 35.3	$2.90^{+1.34}_{-0.95}$	$0.31^{+0.32}_{-0.23}$	5.35/9	0.52 ± 0.12	1.11 ± 0.54	-0.32	0.11	0.766
NGC 1316	3 22 51.22	-37 09 49.5	$3.90^{+1.01}_{-0.78}$	$0.28^{+0.18}_{-0.15}$	8.50/8	1.03 ± 0.10	3.44 ± 1.57	-0.23	-0.30	0.878
NGC 1316	3 23 05.74	-37 11 12.4	$1.42^{+0.36}_{-0.32}$	$0.02^{+0.00}_{-0.00}$	1.10/3	1.30 ± 0.24	1.39 ± 0.24	-0.02	-0.08	0.371
NGC 1399	3 38 20.06	-35 24 45.9	$2.05^{+0.57}_{-0.44}$	$0.08^{+0.12}_{-0.08}$	8.62/9	1.11 ± 0.15	1.31 ± 0.16	-0.18	-0.22	0.351
NGC 1399	3 38 21.90	-35 29 28.3	$1.44^{+0.49}_{-0.33}$	$0.06^{+0.15}_{-0.06}$	4.83/6	1.36 ± 0.19	1.45 ± 0.17	-0.13	0.02	0.268
NGC 1399	3 38 31.82	-35 26 03.8	$3.55^{+0.64}_{-0.52}$	$0.19^{+0.12}_{-0.10}$	17.59/15	1.07 ± 0.10	2.26 ± 0.58	-0.26	-0.37	0.022
NGC 1399	3 38 32.60	-35 27 05.1	$1.51^{+0.12}_{-0.12}$	$0.01^{+0.00}_{-0.00}$	23.76/25	3.53 ± 0.22	3.67 ± 0.24	-0.15	-0.07	0.622
NGC 1407	3 40 08.94	-18 34 47.3	$2.70^{+1.10}_{-0.85}$	$0.38^{+0.45}_{-0.29}$	11.84/7	0.39 ± 0.08	0.83 ± 0.41	-0.39	0.24	0.681
NGC 1407	3 40 11.67	-18 34 56.3	$3.40^{+1.69}_{-1.10}$	$0.19^{+0.29}_{-0.19}$	5.84/8	0.31 ± 0.07	0.67 ± 0.43^d	-0.28	-0.28	0.982
NGC 1407	3 40 14.54	-18 36 37.4	$1.72^{+0.57}_{-0.44}$	$0.10^{+0.14}_{-0.10}$	15.93/12	1.11 ± 0.14	1.30 ± 0.15	-0.11	-0.13	0.306
NGC 1549	4 15 42.40	-55 35 54.6	$2.07^{+0.75}_{-0.60}$	$0.32^{+0.35}_{-0.22}$	9.06/6	1.17 ± 0.21	1.74 ± 0.42	-0.27	0.30	0.918
NGC 1549	4 15 46.40	-55 36 01.9	$1.46^{+0.59}_{-0.43}$	$0.09^{+0.19}_{-0.09}$	4.82/8	1.60 ± 0.24	1.76 ± 0.26	-0.17	0.16	0.115
NGC 1553	4 16 02.71	-55 46 56.2	$2.37^{+0.62}_{-0.51}$	$0.14^{+0.14}_{-0.12}$	7.11/7	1.46 ± 0.16	1.96 ± 0.31	-0.26	-0.13	0.121
NGC 1553	4 16 16.20	-55 46 19.6	$2.00^{+0.73}_{-0.53}$	$0.10^{+0.17}_{-0.10}$	4.24/7	0.82 ± 0.11	0.97 ± 0.13	-0.21	-0.12	0.536
NGC 2403	7 36 25.55	+65 35 40.0	$0.79^{+0.04}_{-0.04}$ b	$0.17^{+0.02}_{-0.02}$	156.00/156	1.73 ± 0.06	1.77 ± 0.04	-0.20	0.28	0.452
UGC 4305	8 19 28.99	+70 42 19.4	$1.72^{+0.34}_{-0.54}$ c	$0.03^{+0.03}_{-0.04}$	93.70/85	4.87 ± 0.22	4.87 ± 0.22	-0.03	0.03	0.992
NGC 2681	8 53 33.65	+51 19 29.5	$2.01^{+0.38}_{-0.21}$	$0.02^{+0.08}_{-0.02}$	5.03/14	0.89 ± 0.09	1.00 ± 0.07	-0.20	-0.14	0.136
NGC 2681	8 53 35.75	+51 19 17.3	$1.46^{+0.57}_{-0.48}$	$1.60^{+0.83}_{-0.58}$	3.82/8	1.82 ± 0.20	2.91 ± 0.52	0.46	0.27	0.184
NGC 3031	9 55 32.98	+69 00 33.4	$1.47^{+0.08}_{-0.09}$ b	$0.17^{+0.05}_{-0.01}$	271.57/255	3.84 ± 0.08	4.39 ± 0.08	0.15	0.21	0.914
NGC 3034	9 55 46.45	+69 40 40.3	$2.47^{+0.20}_{-0.19}$	$0.73^{+0.11}_{-0.10}$	43.05/48	0.48 ± 0.02	1.07 ± 0.09	-0.23	0.50	0.124
NGC 3034	9 55 50.01	+69 40 46.0	$1.17^{+0.15}_{-0.14}$	$0.98^{+0.13}_{-0.12}$	155.87/151	3.85 ± 0.05	20.29 ± 1.18	0.43	0.26	0.722
NGC 3034	9 55 50.57	+69 40 43.2	$2.48^{+0.38}_{-0.42}$ c	$2.33^{+0.33}_{-0.37}$	31.87/34	0.49 ± 0.04	1.35 ± 0.08	0.35	0.31	0.665
NGC 3034	9 55 51.15	+69 40 43.4	$2.50^{+0.64}_{-0.58}$	$21.44^{+4.10}_{-3.58}$	54.56/62	1.87 ± 0.30	23.54 ± 14.51	0.96	0.02	0.349
NGC 3034	9 55 52.13	+69 40 53.2	$2.17^{+0.45}_{-0.41}$	$3.04^{+0.74}_{-0.64}$	28.73/36	0.62 ± 0.04	1.86 ± 0.46	0.58	0.19	0.936
NGC 3034	9 55 54.55	+69 41 00.4	$3.11^{+0.64}_{-0.56}$	$4.97^{+1.31}_{-1.06}$	10.79/15	0.27 ± 0.04	2.85 ± 1.68	0.68	0.16	0.285
NGC 3079	10 02 02.89	+55 38 58.8	$1.65^{+0.30}_{-0.27}$	$0.10^{+0.10}_{-0.09}$	15.82/13	3.45 ± 0.26	3.99 ± 0.33	-0.15	0.11	0.437
NGC 3184	10 18 12.05	+41 24 20.7	$2.04^{+0.32}_{-0.28}$	$0.17^{+0.08}_{-0.07}$	15.50/16	1.69 ± 0.13	2.20 ± 0.17	-0.21	0.02	0.389
NGC 3184	10 18 22.99	+41 27 41.7	$2.03^{+0.26}_{-0.24}$	$0.22^{+0.09}_{-0.08}$	26.69/20	2.09 ± 0.16	2.82 ± 0.23	-0.22	0.14	0.813
NGC 3379	10 47 50.00	+12 34 56.9	$2.55^{+0.29}_{-0.26}$	$0.14^{+0.07}_{-0.06}$	33.88/26	1.50 ± 0.07	2.24 ± 0.20	-0.26	-0.08	0.003
NGC 3379	10 47 50.16	+12 34 55.1	$2.58^{+0.46}_{-0.39}$	$0.22^{+0.11}_{-0.10}$	6.47/11	0.78 ± 0.06	1.29 ± 0.18	-0.27	-0.02	0.664
NGC 3507	11 03 25.71	+18 08 43.8	$1.96^{+0.31}_{-0.28}$	$0.20^{+0.10}_{-0.09}$	11.96/13	2.99 ± 0.28	4.01 ± 0.32	-0.21	0.22	0.169
NGC 3556	11 11 26.05	+55 40 16.9	$2.00^{+0.15}_{-0.14}$	$0.33^{+0.06}_{-0.05}$	52.43/53	4.09 ± 0.17	6.02 ± 0.27	-0.15	0.27	0.722
NGC 3556	11 11 30.34	+55 40 31.3	$1.83^{+0.35}_{-0.31}$	$0.32^{+0.13}_{-0.11}$	11.15/12	1.59 ± 0.14	2.19 ± 0.18	-0.18	0.34	0.390
NGC 3556	11 11 41.41	+55 40 57.8	$2.63^{+0.56}_{-0.49}$	$1.58^{+0.47}_{-0.38}$	5.74/8	1.04 ± 0.09	3.60 ± 1.13	-0.04	0.53	0.022
NGC 3585	11 13 17.84	-26 45 55.0	$1.62^{+0.37}_{-0.34}$	$0.06^{+0.00}_{-0.00}$	2.64/5	0.87 ± 0.17	0.97 ± 0.16	-0.13	0.04	0.607
NGC 3607	11 16 54.64	+18 03 04.1	$4.06^{+3.74}_{-1.43}$	$0.25^{+0.60}_{-0.25}$	3.69/7	0.80 ± 0.29	2.70 ± 5.22	-0.36	-0.04	0.670
NGC 3628	11 20 15.76	+13 35 13.7	$1.67^{+0.11}_{-0.10}$	$0.63^{+0.06}_{-0.06}$	119.08/110	6.66 ± 0.16	9.69 ± 0.28	0.01	0.39	0.018
NGC 3628	11 20 16.25	+13 35 27.2	$1.94^{+0.51}_{-0.45}$	$1.21^{+0.50}_{-0.37}$	3.23/7	0.52 ± 0.06	1.01 ± 0.19	0.12	0.42	0.711
NGC 4038	12 01 51.32	-18 52 25.3	$6.65^{+1.05}_{-1.54}$ c	$0.16^{+0.02}_{-0.03}$	77.82/64	5.99 ± 0.43	6.71 ± 0.28	-0.19	0.27	0.738
NGC 4038	12 01 51.59	-18 52 31.8	$7.11^{+2.89}_{-2.54}$	$0.35^{+0.36}_{-0.32}$	4.45/5	0.20 ± 0.09	2.29 ± 1.36^d	-0.09	-0.83	0.655
NGC 4038	12 01 52.08	-18 51 33.6	$1.16^{+0.05}_{-0.05}$	$0.04^{+0.00}_{-0.00}$	128.70/127	11.46 ± 0.31	12.05 ± 0.30	-0.04	0.09	0.829
NGC 4038	12 01 52.39	-18 52 06.8	$2.55^{+0.35}_{-0.30}$	$0.28^{+0.09}_{-0.08}$	23.49/20	0.91 ± 0.07	1.61 ± 0.16	-0.29	0.08	0.215
NGC 4038	12 01 53.00	-18 52 03.7	$4.62^{+1.86}_{-1.18}$	$0.62^{+0.34}_{-0.24}$	8.08/7	0.21 ± 0.08	2.08 ± 2.06^d	-0.46	0.10	0.434

TABLE 2
Continued

Galaxy	R.A. (h m s)	Decl. (d m s)	Spectral ^a Parameter	n_H (10^{22} cm $^{-2}$)	χ^2/dof	L_{obs} (10^{39} erg s $^{-1}$)	L_{int} (10^{39} erg s $^{-1}$)	($H - M$) color	($M - S$) color	P_{KS}
NGC 4038	12 01 53.50	-18 53 10.7	$4.67^{+1.21}_{-1.90} c$	$0.06^{+0.04}_{-0.03}$	55.86/51	1.89 ± 0.16	2.07 ± 0.10	-0.25	-0.13	0.250
NGC 4038	12 01 54.27	-18 52 01.8	$1.99^{+0.23}_{-0.21}$	$0.09^{+0.06}_{-0.06}$	33.96/27	1.26 ± 0.09	1.53 ± 0.10	-0.20	0.00	0.987
NGC 4038	12 01 54.35	-18 52 10.2	$1.18^{+0.21}_{-0.19}$	$0.07^{+0.07}_{-0.07}$	26.56/25	1.98 ± 0.15	2.13 ± 0.13	-0.02	0.13	0.849
NGC 4038	12 01 54.77	-18 52 52.1	$2.54^{+0.75}_{-0.65}$	$6.51^{+1.67}_{-1.67}$	9.15/13	2.93 ± 0.69	17.86 ± 10.75	0.87	0.07	0.517
NGC 4038	12 01 54.97	-18 53 14.9	$1.69^{+0.12}_{-0.12}$	$0.21^{+0.04}_{-0.04}$	84.34/77	5.42 ± 0.21	6.75 ± 0.19	-0.17	0.24	0.003
NGC 4038	12 01 55.65	-18 52 15.0	$1.26^{+0.11}_{-0.10}$	$0.03^{+0.03}_{-0.03}$	74.89/84	7.26 ± 0.29	7.64 ± 0.23	-0.08	0.06	0.807
NGC 4038	12 01 56.42	-18 51 57.8	$1.95^{+0.11}_{-0.11}$	$0.11^{+0.03}_{-0.03}$	95.67/85	5.09 ± 0.19	6.26 ± 0.20	-0.21	0.03	0.124
NGC 4039	12 01 54.48	-18 53 05.4	$3.23^{+1.34}_{-0.67}$	$0.19^{+0.20}_{-0.11}$	57.82/14	0.40 ± 0.04	0.85 ± 0.29	-0.28	-0.19	0.187
NGC 4125	12 08 01.74	+65 10 34.8	$1.51^{+0.85}_{-0.61}$	$0.12^{+0.19}_{-0.11}$	7.50/6	0.84 ± 0.20	0.93 ± 0.17	-0.10	0.13	0.147
NGC 4125	12 08 07.53	+65 10 28.5	$2.01^{+0.11}_{-0.10}$	$0.02^{+0.00}_{-0.00}$	26.32/38	5.19 ± 0.27	5.88 ± 0.27	-0.20	-0.15	0.208
NGC 4125	12 08 17.44	+65 11 25.3	$1.21^{+0.57}_{-0.30}$	$0.03^{+0.17}_{-0.03}$	7.46/8	1.23 ± 0.22	1.28 ± 0.18	0.01	0.04	0.984
NGC 4151	12 10 22.37	+39 23 16.9	$1.89^{+0.19}_{-0.18}$	$0.02^{+0.00}_{-0.00}$	4.97/10	1.34 ± 0.11	1.42 ± 0.12	-0.17	-0.21	0.112
NGC 4258	12 18 43.86	+47 17 31.5	$1.81^{+0.31}_{-0.28}$	$0.15^{+0.10}_{-0.09}$	10.71/14	1.06 ± 0.08	1.30 ± 0.11	-0.22	0.17	0.349
NGC 4258	12 18 57.84	+47 16 07.1	$2.00^{+0.28}_{-0.19}$	$0.51^{+0.10}_{-0.09}$	28.01/32	2.61 ± 0.16	4.22 ± 0.27	-0.14	0.38	0.528
NGC 4303	12 21 55.46	+04 28 58.4	$1.88^{+0.92}_{-0.75}$	$0.30^{+0.28}_{-0.19}$	6.25/8	1.14 ± 0.27	1.58 ± 0.23	-0.29	0.35	0.492
NGC 4303	12 21 56.57	+04 29 24.4	$3.13^{+1.15}_{-0.88}$	$0.28^{+0.27}_{-0.21}$	9.20/6	0.47 ± 0.10	1.11 ± 0.51^d	-0.43	0.11	0.147
NGC 4303	12 21 58.34	+04 28 12.2	$3.23^{+1.07}_{-0.72}$	$0.34^{+0.22}_{-0.16}$	7.76/10	0.63 ± 0.08	1.71 ± 0.67	-0.30	-0.01	0.748
NGC 4303	12 22 01.25	+04 29 37.4	$1.98^{+0.24}_{-0.22}$	$0.02^{+0.00}_{-0.00}$	4.41/7	1.64 ± 0.18	1.85 ± 0.17	-0.22	-0.08	0.016
NGC 4365	12 24 26.39	+07 16 53.3	$1.35^{+0.44}_{-0.39}$	$0.33^{+0.21}_{-0.17}$	4.82/6	2.67 ± 0.27	3.27 ± 0.32	-0.01	0.34	0.289
NGC 4365	12 24 28.45	+07 19 05.9	$2.04^{+0.39}_{-0.35}$	$0.02^{+0.00}_{-0.00}$	2.96/7	0.65 ± 0.11	0.83 ± 0.21	-0.16	-0.17	0.247
NGC 4365	12 24 38.29	+07 21 06.8	$3.29^{+1.62}_{-0.94}$	$0.14^{+0.28}_{-0.14}$	2.83/5	0.47 ± 0.10	0.90 ± 0.54^d	-0.28	-0.23	0.000
NGC 4374	12 25 03.48	+12 53 19.2	$1.89^{+0.83}_{-0.52}$	$0.09^{+0.26}_{-0.09}$	6.59/8	0.71 ± 0.12	0.83 ± 0.17	-0.28	0.04	0.434
NGC 4382	12 25 17.17	+18 13 46.7	$2.24^{+0.17}_{-0.17}$	$0.03^{+0.00}_{-0.00}$	14.01/16	2.28 ± 0.17	2.68 ± 0.16	-0.20	-0.23	0.413
NGC 4382	12 25 20.32	+18 13 01.6	$2.96^{+0.84}_{-0.65}$	$0.28^{+0.23}_{-0.18}$	7.41/10	0.73 ± 0.10	1.59 ± 0.52	-0.41	0.09	0.390
NGC 4388	12 25 38.95	+12 40 00.9	$2.29^{+0.90}_{-0.66}$	$0.15^{+0.25}_{-0.15}$	1.80/5	0.87 ± 0.17	1.24 ± 0.32	-0.25	0.04	0.335
NGC 4388	12 25 39.10	+12 40 09.5	$2.13^{+0.61}_{-0.50}$	$0.13^{+0.18}_{-0.13}$	9.04/8	1.24 ± 0.19	1.63 ± 0.28	-0.22	0.02	0.867
NGC 4395	12 25 39.51	+33 32 04.3	$5.11^{+1.73}_{-1.26}$	$0.45^{+0.29}_{-0.22}$	6.52/5	0.07 ± 0.02	0.62 ± 0.61^d	-0.31	-0.24	0.100
NGC 4449	12 28 17.83	+44 06 33.9	$1.99^{+0.16}_{-0.16}$	$0.57^{+0.08}_{-0.07}$	54.19/56	0.75 ± 0.03	1.22 ± 0.06	-0.16	0.41	0.928
NGC 4472	12 29 34.46	+07 58 51.6	$1.72^{+0.24}_{-0.23}$	$0.02^{+0.00}_{-0.00}$	2.18/6	1.26 ± 0.15	1.33 ± 0.15	-0.15	0.11	0.144
NGC 4472	12 29 34.49	+08 00 32.3	$1.82^{+0.52}_{-0.44}$	$0.22^{+0.17}_{-0.14}$	4.72/10	0.89 ± 0.13	1.16 ± 0.15	-0.17	0.13	0.978
NGC 4472	12 29 40.99	+07 57 44.2	$2.71^{+0.67}_{-0.53}$	$0.37^{+0.22}_{-0.17}$	11.22/9	0.76 ± 0.10	1.55 ± 0.41	-0.27	0.24	0.260
NGC 4472	12 29 42.31	+08 00 08.0	$1.68^{+0.50}_{-0.43}$	$0.12^{+0.15}_{-0.12}$	0.24/5	0.93 ± 0.13	1.09 ± 0.12	-0.14	0.01	0.386
NGC 4485	12 30 30.56	+41 41 42.3	$1.08^{+0.05}_{-0.17} b$	$0.16^{+0.04}_{-0.03}$	52.35/54	5.70 ± 0.21	6.34 ± 0.28	-0.13	0.24	0.505
NGC 4490	12 30 29.55	+41 39 27.6	$3.38^{+0.70}_{-0.58}$	$2.59^{+0.80}_{-0.62}$	21.85/22	0.98 ± 0.13	9.67 ± 5.62	0.10	0.44	0.946
NGC 4490	12 30 30.82	+41 39 11.5	$2.05^{+0.26}_{-0.24}$	$1.00^{+0.17}_{-0.15}$	22.82/28	2.63 ± 0.17	5.10 ± 0.46	-0.01	0.46	0.673
NGC 4490	12 30 32.27	+41 39 18.1	$1.79^{+0.26}_{-0.23}$	$0.40^{+0.11}_{-0.10}$	14.71/21	1.69 ± 0.13	2.36 ± 0.16	-0.13	0.37	0.618
NGC 4490	12 30 36.32	+41 38 37.8	$1.93^{+0.26}_{-0.24}$	$0.55^{+0.12}_{-0.10}$	19.66/22	1.76 ± 0.14	2.77 ± 0.20	-0.11	0.38	0.810
NGC 4490	12 30 43.25	+41 38 18.4	$0.80^{+0.07}_{-0.08} b$	$1.04^{+0.14}_{-0.15}$	35.57/37	3.14 ± 0.21	6.23 ± 0.35	-0.11	0.41	0.761
NGC 4486	12 30 47.12	+12 24 15.8	$3.20^{+0.53}_{-0.43}$	$0.26^{+0.11}_{-0.09}$	16.88/18	1.43 ± 0.13	3.25 ± 0.65	-0.32	-0.13	0.004
NGC 4486	12 30 49.24	+12 23 34.5	$3.53^{+2.84}_{-1.04}$	$0.14^{+0.72}_{-0.14}$	17.30/21	0.42 ± 0.15	0.80 ± 1.48^d	-0.19	-0.44	0.867
NGC 4486	12 30 49.18	+12 26 04.2	$2.07^{+0.66}_{-0.40}$	$0.06^{+0.14}_{-0.06}$	3.47/10	0.90 ± 0.14	1.06 ± 0.14	-0.18	-0.18	0.745
NGC 4486	12 30 50.79	+12 25 01.8	$1.94^{+0.55}_{-0.42}$	$0.08^{+0.12}_{-0.08}$	16.67/18	1.26 ± 0.15	1.48 ± 0.15	-0.14	-0.01	0.473
NGC 4486	12 30 50.90	+12 23 25.0	$4.26^{+5.74}_{-2.06}$	$0.40^{+0.88}_{-0.37}$	3.77/9	0.26 ± 0.13	1.28 ± 9.42^d	-0.38	-0.14	0.353
NGC 4486	12 30 53.24	+12 23 56.8	$0.16^{+0.07}_{-0.13} c$	$0.38^{+0.38}_{-0.61}$	22.59/14	0.50 ± 0.13	1.74 ± 0.20	-0.10	-0.10	0.431
NGC 4494	12 31 28.58	+25 44 57.6	$1.76^{+0.30}_{-0.27}$	$0.01^{+0.00}_{-0.00}$	5.56/5	1.05 ± 0.13	1.16 ± 0.15	-0.16	-0.16	0.921
NGC 4494	12 31 29.62	+25 46 21.9	$2.59^{+0.67}_{-0.48}$	$0.08^{+0.14}_{-0.08}$	2.97/7	1.32 ± 0.15	1.87 ± 0.33	-0.23	-0.22	0.491
NGC 4552	12 35 41.22	+12 34 51.5	$1.63^{+0.57}_{-0.49}$	$0.11^{+0.16}_{-0.11}$	12.61/10	1.34 ± 0.23	1.57 ± 0.17	-0.16	0.07	0.446
NGC 4552	12 35 44.82	+12 33 40.8	$1.15^{+0.15}_{-0.73} b$	$0.35^{+0.35}_{-0.75}$	8.60/08	0.57 ± 0.07	0.93 ± 0.14	-0.08	-0.03	0.947
NGC 4552	12 35 45.77	+12 33 02.4	$2.65^{+0.54}_{-0.44}$	$0.27^{+0.13}_{-0.11}$	11.64/10	0.82 ± 0.08	1.51 ± 0.24	-0.34	0.11	0.445
NGC 4559	12 35 51.71	+27 56 04.1	$3.12^{+0.59}_{-0.85} c$	$0.02^{+0.02}_{-0.04}$	75.81/67	9.41 ± 0.79	9.83 ± 0.38	-0.20	-0.14	0.812
NGC 4559	12 35 57.80	+27 58 07.2	$2.28^{+0.49}_{-0.43}$	$0.29^{+0.18}_{-0.14}$	10.31/7	1.80 ± 0.19	2.89 ± 0.46	-0.28	0.22	0.716
NGC 4559	12 35 58.57	+27 57 41.8	$1.80^{+0.15}_{-0.14}$	$0.14^{+0.05}_{-0.05}$	58.71/49	11.07 ± 0.59	13.60 ± 0.58	-0.19	0.15	0.693
NGC 4579	12 37 40.30	+11 47 27.5	$1.89^{+0.14}_{-0.13}$	$0.15^{+0.04}_{-0.04}$	65.78/58	16.29 ± 0.63	20.21 ± 0.75	-0.17	0.04	0.526
NGC 4579	12 37 43.20	+11 49 01.2	$1.69^{+0.30}_{-0.28}$	$0.02^{+0.00}_{-0.00}$	8.63/8	1.52 ± 0.19	1.65 ± 0.20	-0.18	-0.05	0.734
NGC 4579	12 37 53.89	+11 50 20.1	$2.03^{+0.58}_{-0.40}$	$0.07^{+0.15}_{-0.07}$	8.38/10	1.37 ± 0.21	1.60 ± 0.25	-0.23	-0.05	0.009

TABLE 2
Continued

Galaxy	R.A. (h m s)	Decl. (d m s)	Spectral ^a Parameter	n_H (10^{22} cm^{-2})	χ^2/dof	L_{obs} ($10^{39} \text{ erg s}^{-1}$)	L_{int} ($10^{39} \text{ erg s}^{-1}$)	($H - M$) color	($M - S$) color	P_{KS}
NGC 4594	12 40 00.97	-11 36 54.2	$2.52^{+0.47}_{-0.41}$	$0.18^{+0.13}_{-0.11}$	8.43/9	0.91 ± 0.08	1.44 ± 0.23	-0.30	0.05	0.352
NGC 4594	12 40 01.10	-11 37 24.2	$5.62^{+1.49}_{-1.13}$	$0.36^{+0.22}_{-0.17}$	7.55/12	0.66 ± 0.13	5.73 ± 4.64^d	-0.22	-0.53	0.096
NGC 4621	12 42 02.99	+11 41 16.3	$1.59^{+0.71}_{-0.58}$	$0.21^{+0.24}_{-0.19}$	4.93/5	1.00 ± 0.18	1.24 ± 0.17	-0.03	0.20	0.938
NGC 4631	12 41 55.56	+32 32 16.9	$1.75^{+0.38}_{-0.35}$	$0.16^{+0.03}_{-0.03}$	134.36/105	2.42 ± 0.10	2.94 ± 0.08	-0.18	0.14	0.599
NGC 4631	12 42 11.13	+32 32 35.8	$2.79^{+0.38}_{-0.35}$	$3.99^{+0.63}_{-0.56}$	44.86/47	2.20 ± 0.12	13.81 ± 3.96	0.57	0.20	0.228
NGC 4649	12 43 32.08	+11 34 18.5	$2.33^{+0.76}_{-0.62}$	$0.67^{+0.38}_{-0.27}$	3.12/6	0.86 ± 0.14	1.73 ± 0.47	-0.16	0.40	0.164
NGC 4649	12 43 37.27	+11 31 43.7	$1.85^{+0.25}_{-0.22}$	$0.02^{+0.00}_{-0.00}$	4.91/7	0.97 ± 0.11	1.04 ± 0.12	-0.15	-0.26	0.016
NGC 4649	12 43 45.00	+11 32 33.4	$1.53^{+0.28}_{-0.26}$	$0.02^{+0.00}_{-0.00}$	14.13/11	0.90 ± 0.11	0.93 ± 0.14	-0.10	-0.10	0.986
NGC 4697	12 48 46.83	-05 48 53.5	$1.68^{+0.37}_{-0.33}$	$0.14^{+0.12}_{-0.10}$	14.21/9	1.00 ± 0.10	1.16 ± 0.11	-0.25	0.06	0.246
NGC 4736	12 50 52.72	+41 07 19.0	$1.82^{+0.12}_{-0.11}$	$0.04^{+0.03}_{-0.03}$	83.76/81	0.86 ± 0.03	0.95 ± 0.03	-0.15	-0.13	0.086
NGC 4945	13 05 21.94	-49 28 26.6	$1.09^{+0.06 b}_{-0.06}$	$0.44^{+0.04}_{-0.04}$	97.11/110	0.77 ± 0.02	1.04 ± 0.03	-0.16	0.41	0.458
NGC 4945	13 05 32.89	-49 27 34.1	$1.81^{+0.12}_{-0.11}$	$0.76^{+0.08}_{-0.07}$	113.59/101	0.95 ± 0.03	1.52 ± 0.05	0.02	0.39	0.187
NGC 5055	13 15 19.55	+42 03 02.3	$2.51^{+0.15}_{-0.14}$	$0.18^{+0.04}_{-0.04}$	96.01/83	13.45 ± 0.49	21.28 ± 0.95	-0.29	0.04	0.011
NGC 5055	13 15 39.33	+42 01 53.4	$2.30^{+0.37}_{-0.32}$	$0.54^{+0.26}_{-0.20}$	2.91/5	0.57 ± 0.07	1.07 ± 0.21	-0.31	0.46	0.780
NGC 5055	13 16 02.27	+42 01 53.6	$3.52^{+0.37}_{-0.32}$	$0.56^{+0.11}_{-0.10}$	21.85/23	1.29 ± 0.09	5.56 ± 1.06	-0.49	0.36	0.000
NGC 5204	13 29 38.61	+58 25 05.6	$2.99^{+0.25}_{-0.22}$	$0.10^{+0.05}_{-0.05}$	45.10/41	1.20 ± 0.05	1.90 ± 0.17	-0.26	-0.28	0.443
NGC 5194	13 29 43.29	+47 11 34.7	$0.11^{+0.04 b}_{-0.03}$	$0.22^{+0.18}_{-0.30}$	3.64/6	0.23 ± 0.10	1.65 ± 0.20	-0.05	-0.91	0.071
NGC 5194	13 29 50.67	+47 11 55.0	$1.86^{+0.75}_{-0.64}$	$3.75^{+1.55}_{-1.19}$	7.69/9	2.21 ± 0.28	5.58 ± 2.03	0.75	0.13	0.740
NGC 5194	13 29 53.31	+47 10 42.3	$1.55^{+0.14}_{-0.13}$	$0.01^{+0.00}_{-0.00}$	20.79/23	1.67 ± 0.11	1.81 ± 0.12	-0.13	-0.01	0.511
NGC 5194	13 29 53.73	+47 14 35.6	$1.33^{+0.27}_{-0.18}$	$0.02^{+0.08}_{-0.02}$	10.63/14	1.56 ± 0.15	1.65 ± 0.13	-0.10	0.05	0.802
NGC 5194	13 29 57.56	+47 10 48.3	$2.32^{+0.46}_{-0.40}$	$0.19^{+0.13}_{-0.11}$	11.24/9	0.65 ± 0.07	0.98 ± 0.13	-0.30	0.14	0.496
NGC 5194	13 29 59.53	+47 15 58.5	$4.47^{+2.17 c}_{-19.79}$	$0.87^{+0.30}_{-0.21}$	20.63/24	0.94 ± 0.01	3.50 ± 0.32	-0.14	0.10	0.036
NGC 5194	13 30 07.56	+47 11 05.6	$1.83^{+0.11}_{-0.10}$	$0.01^{+0.00}_{-0.00}$	35.78/34	2.28 ± 0.13	2.52 ± 0.12	-0.19	-0.06	0.152
NGC 5457	14 02 29.89	+54 21 19.0	$0.15^{+0.06 c}_{-0.06}$	$0.18^{+0.10}_{-0.19}$	95.74/89	0.81 ± 0.12	1.43 ± 0.05	-0.32	-0.14	0.000
NGC 5457	14 03 32.38	+54 21 03.0	$3.56^{+0.15}_{-0.14}$	$0.35^{+0.04}_{-0.03}$	154.31/148	2.05 ± 0.05	6.43 ± 0.46	-0.44	0.21	0.000
NGC 5457	14 04 14.28	+54 26 03.6	$0.11^{+0.01 b}_{-0.00}$	$0.31^{+0.02}_{-0.01}$	97.79/87	1.23 ± 0.04	1.57 ± 0.04	-0.10	-0.78	0.282
Circinus	14 12 53.52	-65 22 54.7	$3.10^{+0.31}_{-0.28}$	$0.87^{+0.15}_{-0.13}$	28.10/23	0.38 ± 0.03	1.50 ± 0.26^d	-0.37	0.50	0.624
Circinus	14 13 10.05	-65 20 44.8	$1.47^{+0.16}_{-0.15}$	$0.92^{+0.13}_{-0.11}$	111.28/69	1.84 ± 0.07	2.65 ± 0.11	0.22	0.35	0.999
Circinus	14 13 12.24	-65 20 14.0	$0.88^{+0.14}_{-0.13}$	$0.82^{+0.14}_{-0.13}$	115.55/106	3.72 ± 0.12	4.49 ± 0.19	0.38	0.28	0.000
NGC 5774	14 53 39.95	+03 34 18.9	$1.46^{+0.48}_{-0.42}$	$0.20^{+0.19}_{-0.16}$	6.78/5	2.28 ± 0.35	2.72 ± 0.30	-0.14	0.31	0.000
NGC 5774	14 53 43.77	+03 34 27.1	$2.21^{+1.23}_{-0.97}$	$0.38^{+0.48}_{-0.34}$	1.39/2	0.53 ± 0.13	0.90 ± 0.34	-0.32	0.39	0.004
NGC 5775	14 53 55.76	+03 33 28.1	$1.58^{+0.74}_{-0.29}$	$1.55^{+1.07}_{-0.67}$	6.63/7	4.50 ± 0.48	7.52 ± 1.83	0.43	0.25	0.709
NGC 5775	14 53 58.89	+03 32 16.8	$1.76^{+0.26}_{-0.24}$	$2.44^{+0.40}_{-0.35}$	52.00/50	31.28 ± 1.19	64.75 ± 6.67	0.56	0.21	0.393
NGC 5775	14 53 59.45	+03 31 57.3	$1.48^{+0.36}_{-0.32}$	$0.50^{+0.23}_{-0.18}$	9.49/11	4.98 ± 0.59	6.59 ± 0.61	0.04	0.34	0.893
NGC 5775	14 54 00.97	+03 31 33.1	$0.78^{+0.58}_{-0.61}$	$0.81^{+1.00}_{-0.55}$	5.69/10	3.61 ± 0.59	4.30 ± 0.60	0.48	0.19	0.039
NGC 6946	20 34 36.48	+60 09 30.4	$4.25^{+0.51}_{-0.41}$	$0.40^{+0.09}_{-0.08}$	52.19/30	0.19 ± 0.01	0.98 ± 0.23	-0.36	-0.10	0.247
NGC 6946	20 34 52.30	+60 09 11.7	$2.62^{+0.21}_{-0.19}$	$0.75^{+0.10}_{-0.09}$	44.77/36	0.53 ± 0.03	1.36 ± 0.13	-0.24	0.44	0.219
NGC 6946	20 34 56.49	+60 08 34.0	$3.94^{+1.17 c}_{-1.65}$	$1.55^{+0.45}_{-0.32}$	35.81/30	0.24 ± 0.02	1.22 ± 0.11	0.00	0.31	0.011
NGC 6946	20 35 00.74	+60 11 30.6	$0.67^{+0.08 c}_{-0.17}$	$0.15^{+0.03}_{-0.02}$	171.39/153	3.28 ± 0.15	4.15 ± 0.07	-0.26	0.02	0.395
NGC 6946	20 35 18.79	+60 10 56.2	$3.47^{+0.46}_{-0.39}$	$1.35^{+0.34}_{-0.26}$	24.39/19	0.29 ± 0.03	2.10 ± 0.69	-0.26	0.53	0.421
NGC 7331	22 37 05.64	+34 26 53.5	$2.34^{+0.66}_{-0.55}$	$0.71^{+0.38}_{-0.27}$	5.62/8	1.13 ± 0.19	2.36 ± 0.62	-0.14	0.44	0.629
NGC 7331	22 37 06.62	+34 26 20.1	$2.26^{+0.63}_{-0.52}$	$0.69^{+0.31}_{-0.24}$	5.08/5	1.41 ± 0.20	2.80 ± 0.60	-0.23	0.48	0.075
NGC 7331	22 37 08.08	+34 26 00.2	$2.24^{+0.55}_{-0.46}$	$0.29^{+0.16}_{-0.14}$	5.82/5	1.17 ± 0.13	1.84 ± 0.27	-0.29	0.23	0.060
IC 1459	22 57 09.51	-36 28 24.0	$1.70^{+0.36}_{-0.32}$	$0.01^{+0.00}_{-0.00}$	5.80/9	0.81 ± 0.14	0.91 ± 0.13	-0.06	-0.09	0.577
IC 1459	22 57 20.73	-36 27 47.2	$2.63^{+0.73}_{-0.56}$	$0.20^{+0.17}_{-0.14}$	7.21/11	0.84 ± 0.11	1.43 ± 0.31	-0.24	-0.02	0.887

^aPower-law index, Γ , unless otherwise noted.^bDisk-blackbody model inner disk temperature, kT_{in} , in keV.^cThermal emission-line model temperature, kT , in keV.^dIntrinsic luminosity $< 10^{39} \text{ ergs s}^{-1}$ when fit using a thermal emission-line model.

TABLE 3
LINEAR CORRELATION COEFFICIENTS^a

	All Galaxies			Subsample		
	All	Ellip.	Spiral	All	Ellip.	Spiral
$N_{\text{ULX}}, L_{\text{B}}$	0.74	0.89	—	0.70	(0.89)	0.71
$N_{\text{ULX}}, L_{\text{FIR}}$	0.63	—	0.88	(0.50)	—	0.71
N_{ULX}, θ_p	—	—	(-.54)	—	—	—
$L_{\text{ULX}}, L_{\text{B}}$	—	0.82	—	—	—	0.76
$L_{\text{ULX}}, L_{\text{FIR}}$	0.57	—	0.88	0.83	—	0.80
L_{ULX}, θ_p	—	—	(-.54)	—	—	—
$L_{\text{ULX}}/N_{\text{ULX}}, L_{\text{B}}$	—	0.86	—	—	—	0.82
$L_{\text{ULX}}/N_{\text{ULX}}, L_{\text{FIR}}$	—	—	0.82	0.92	—	0.91
$L_{\text{ULX}}/L_{\text{B}}, L_{\text{FIR}}/L_{\text{B}}$	0.80	—	0.99	—	—	—
$N_{\text{ULX}}/L_{\text{B}}, L_{\text{FIR}}/L_{\text{B}}$	0.56	—	0.97	—	—	—
$(L_{\text{ULX}}/N_{\text{ULX}})/L_{\text{B}}, L_{\text{FIR}}/L_{\text{B}}$	—	—	0.90	—	—	—

^a() denote marginally significant correlation, — denotes no correlation